

NEBULAR EXCITATION IN $z \sim 2$ STAR-FORMING GALAXIES FROM THE SINS AND LUCI SURVEYS: THE INFLUENCE OF SHOCKS AND ACTIVE GALACTIC NUCLEI*

SARAH F. NEWMAN¹, PETER BUSCHKAMP², REINHARD GENZEL^{1,2,3}, NATASCHA M. FÖRSTER SCHREIBER², JARON KURK²,
 AMIEL STERNBERG⁴, ORLY GNAT⁵, DAVID ROSARIO², CHIARA MANCINI⁶, SIMON J. LILLY⁷, ALVIO RENZINI⁶, ANDREAS BURKERT⁸,
 C. MARCELLA CAROLLO⁷, GIOVANNI CRESCI⁹, RIC DAVIES², FRANK EISENHAEUER², SHY GENEL¹⁰, KRISTEN SHAPIRO GRIFFIN¹¹,
 ERIN K. S. HICKS¹², DIETER LUTZ², THORSTEN NAAB¹³, YINGJIE PENG⁷, LINDA J. TACCONI², STIJN WUYTS², GIANNI ZAMORANI¹⁴,
 DANIELA VERGANI¹⁵, AND BENJAMIN J. WEINER¹⁶

¹ Department of Astronomy, Campbell Hall, University of California, Berkeley, CA 94720, USA; sfnewman@berkeley.edu

² Max-Planck-Institut für extraterrestrische Physik (MPE), Giessenbachstr. 1, D-85748 Garching, Germany

³ Department of Physics, Le Conte Hall, University of California, Berkeley, CA 94720, USA

⁴ School of Physics and Astronomy, Tel Aviv University, Tel Aviv 69978, Israel

⁵ Racah Institute of Physics, The Hebrew University, Jerusalem 91904, Israel

⁶ Osservatorio Astronomico di Padova, Vicolo dell'Osservatorio 5, I-35122 Padova, Italy

⁷ Institute of Astronomy, Department of Physics, Eidgenössische Technische Hochschule, ETH, CH-8093 Zürich, Switzerland

⁸ Universitäts-Sternwarte Ludwig-Maximilians-Universität (USM), Scheinerstr. 1, D-81679 München, Germany

⁹ Istituto Nazionale di Astrofisica Osservatorio di Bologna, Via Ranzani 1, I-40127 Bologna, Italy

¹⁰ Harvard-Smithsonian Center for Astrophysics, 60 Garden Street, Cambridge, MA 02138, USA

¹¹ Space Sciences Research Group, Northrop Grumman Aerospace Systems, Redondo Beach, CA 90278, USA

¹² Department of Astronomy, University of Washington, Box 351580, U.W., Seattle, WA 98195-1580, USA

¹³ Max-Planck Institute for Astrophysics, Karl Schwarzschildstrasse 1, D-85748 Garching, Germany

¹⁴ INAF Osservatorio Astronomico di Bologna, Via Ranzani 1, I-40127 Bologna, Italy

¹⁵ INAF Istituto di Astrofisica Spaziale e Fisica Cosmica di Bologna, Via P. Gobetti 101, I-40129 Bologna, Italy

¹⁶ Steward Observatory, University of Arizona, Tucson, AZ 85721, USA

Received 2013 June 27; accepted 2013 December 2; published 2013 December 31

ABSTRACT

Based on high-resolution, spatially resolved data of 10 $z \sim 2$ star-forming galaxies from the SINS/zC-SINF survey and LUCI data for 12 additional galaxies, we probe the excitation properties of high- z galaxies and the impact of active galactic nuclei (AGNs), shocks, and photoionization. We explore how these spatially resolved line ratios can inform our interpretation of integrated emission line ratios obtained at high redshift. Many of our galaxies fall in the “composite” region of the $z \sim 0$ [N II]/H α versus [O III]/H β diagnostic (BPT) diagram, between star-forming galaxies and those with AGNs. Based on our resolved measurements, we find that some of these galaxies likely host an AGN, while others appear to be affected by the presence of shocks possibly caused by an outflow or from an enhanced ionization parameter as compared with H II regions in normal, local star-forming galaxies. We find that the Mass-Excitation (MEx) diagnostic, which separates purely star-forming and AGN hosting local galaxies in the [O III]/H β versus stellar mass plane, does not properly separate $z \sim 2$ galaxies classified according to the BPT diagram. However, if we shift the galaxies based on the offset between the local and $z \sim 2$ mass–metallicity relation (i.e., to the mass they would have at $z \sim 0$ with the same metallicity), we find better agreement between the MEx and BPT diagnostics. Finally, we find that metallicity calibrations based on [N II]/H α are more biased by shocks and AGNs at high- z than the [O III]/H β /[N II]/H α calibration.

Key words: galaxies: evolution – galaxies: high-redshift – infrared: galaxies

Online-only material: color figures

1. INTRODUCTION

Optical and near-infrared (NIR) surveys over the last 15 yr have firmly established that star-forming galaxies (SFGs) at $z \sim 2$ have very different morphological structure in their rest-frame UV/optical light than their local counterparts (e.g., Cowie et al. 1995; van den Bergh et al. 1996; Elmegreen et al. 2004, 2009; Elmegreen & Elmegreen 2005, 2006; Genzel et al. 2006, 2008, 2011; Law et al. 2007, 2009, 2012; Förster Schreiber et al. 2009, 2011a; Wuyts et al. 2012; Swinbank et al. 2012a, 2012b; Jones et al. 2010, 2012). Although a majority are characterized as rotating disks with kinematic analysis, they exhibit clumpy

structure and elevated velocity dispersions, indicating much larger scale heights than local disks (Elmegreen & Elmegreen 2006; Förster Schreiber et al. 2006, 2009; Law et al. 2007, 2009; Genzel et al. 2008, 2011; Wright et al. 2007, 2009; Shapiro et al. 2008; Cresci et al. 2009; van Starkenburg et al. 2008; Epinat et al. 2009; Lemoine-Busserolle & Lamareille 2010; Jones et al. 2012; Wisnioski et al. 2012; Swinbank et al. 2012a, 2012b; Epinat et al. 2012; Newman et al. 2013). In addition, their star formation rates (SFRs), star formation rate surface densities (Σ_{SFR}), and interstellar pressures are more similar to those of local starbursting galaxies than local normal star-forming disks (Newman et al. 2012).

Given the differing physical conditions in local and high- z SFGs, one might expect this to be reflected in their nebular excitation properties. Indeed, high- z SFGs often fall in the “composite” region of the BPT (Baldwin et al. 1981) diagram (the plane of [O III]/H β versus [N II]/H α), between H II regions

* Based on observations at the Very Large Telescope (VLT) of the European Southern Observatory (ESO), Paranal, Chile (ESO program IDs 073.B-9018, 076.A-0527, 079.A-0341, 080.A-0330, 080.A-0339, 080.A-0635, 083.A-0781, 084.A-0853, 087.A-0081, 091.A-0126) and at the Large Binocular Telescope (LBT) on Mt. Graham in Arizona.

and active galactic nuclei (AGNs), coincident with the location of many local starburst galaxies (Tecza et al. 2004; Shapley et al. 2005; Kewley et al. 2006; Erb et al. 2006a; Liu et al. 2008; Trump et al. 2013; Juneau et al. 2011; Kriek et al. 2007; Hayashi et al. 2009; Yabe et al. 2012; Yuan et al. 2013b). In fact, Liu et al. (2008) and Brinchmann et al. (2008) have found, among local Sloan Digital Sky Survey (SDSS) galaxies, a positive correlation between relative offset from the main star-forming H II branch of the BPT diagram toward the “composite” region and ionization parameter, SFR, and electron density. They have suggested that higher values of these galaxy parameters could explain the position of high- z galaxies in the BPT diagram as well. Conversely, the offset of $z \sim 2$ galaxies from the star-forming branch of the BPT diagram could also be due to the presence of AGNs or shocks from large-scale outflows. Unfortunately, weak AGNs can be difficult to identify in integrated line ratios, but spatially resolved data can help to uncover them as demonstrated by the case study of a $z = 1.6$ galaxy by Wright et al. (2009, 2010). More recently, Newman et al. (2012) found that for two star-forming clumps in a $z \sim 2$ SFG, elevated [N II]/H α and [S II]/H α ratios were at least in part due to shocks from a galactic-scale outflow originating from the clumps, with no evidence for an underlying AGN. Determining the cause(s) of the offset of high- z galaxies in the BPT diagram is instrumental for understanding the physical properties of these objects and in particular the contribution of AGNs to their evolution.

In addition to understanding the physical properties of these galaxies, quantifying the effects of shocks and AGNs on emission line ratios will help us to better estimate their gas phase metallicity. These metallicities are essential for properly understanding the interplay between gas inflow, outflow, and star formation at the peak epoch of the SFR density at $z \sim 2-3$ (Lilly et al. 2013). Rest-optical nebular line ratios calibrated locally are the main technique used for measuring metallicity at high- z . However, different diagnostics can give very different results (see e.g., Kewley & Ellison 2008), and if the [N II]/H α ratio is indeed elevated in many high- z galaxies by either the physical conditions in H II regions, the presence of shocks, or an AGN, metallicities determined using this ratio could be systematically overestimated.

In this work, we present K -, H -, and/or J -band datasets for 22 $z \sim 1.4-2.5$ rest-UV/optically selected SFGs obtained as part of the SINS/zC-SINF and LUCI surveys (Förster Schreiber et al. 2009; Mancini et al. 2011; J. Kurk et al. 2013, in preparation). Thus for each galaxy, we measure H α , [N II], [O III], and H β fluxes. The faintness of these lines and the requirement that all, or a significant subset of them, should be observable between the bright night sky OH lines in the NIR atmospheric windows make such studies from the ground very challenging. The SINS/zC-SINF and LUCI surveys allowed us to cull a sizeable amount of suitable targets for a first exploration of spatially resolved metallicities and excitation in massive $z \sim 2$ SFGs. We adopt a Λ CDM cosmology with $\Omega_m = 0.27$, $\Omega_b = 0.046$, and $H_0 = 70 \text{ km s}^{-1} \text{ Mpc}^{-1}$ (Komatsu et al. 2011), as well as a Chabrier (2003) initial stellar mass function (IMF).

2. OBSERVATIONS AND ANALYSIS

2.1. Source Selection, Observations, and Data Reduction of SINS/zC-SINF Galaxies

Half of our sample (10 SFGs) was drawn from the SINS and zC-SINF surveys of IFU spectroscopic data of $z \sim 1.5-2.5$ SFGs, obtained using SINFONI on the Very Large Telescope

(VLT) of the European Southern Observatory (ESO). For all of these objects, we obtained either K - and H -band (for $z = 2-2.5$) or H - and J -band (for $z = 1.4$) data in the seeing-limited mode of SINFONI. For a subset of these objects (six), we also obtained K -band data in the AO mode with the aid of either a natural or laser guide star. The seeing-limited data have a pixel scale of $0''.125 \times 0''.25$, whereas the AO data have a pixel scale of $0''.05 \times 0''.1$, with a spectral resolution of $R = 1900, 2900$, and 4500 (5000) for the J -, H -, and K -band (AO), respectively.

The full SINS and zC-SINF samples were selected as described in Förster Schreiber et al. (2009) and Mancini et al. (2011). Of the final 10 galaxies used in this analysis, two were selected based on their K -band magnitudes (Daddi et al. 2004; Mignoli et al. 2005), three based on their K -band magnitudes and BzK colors (Kong et al. 2006; Lilly et al. 2007), and five from their U_n GR colors (Erb et al. 2003; Adelberger et al. 2004; Steidel et al. 2004; Erb et al. 2006b; Law et al. 2009).

We further selected galaxies to be observed in the H - or J -band based on the requirement that they fall at a redshift such that all four emission lines of interest ([N II], H α , [O III], H β) are unaffected or weakly affected by OH sky lines. In addition, these targets are among the brighter objects in the SINS sample, enabling us to observe the relatively weak H β and [O III] lines in comparatively short exposure times. For the present study, we included only galaxies that had a secure detection in all four emission lines with minimal interference from an OH sky line or had a secure detection in three lines and an upper limit for one of the lines, with the requirement that there was not an OH sky line near the upper limit, in order to ensure a meaningful value. Out of 15 galaxies for which we attempted to measure all four lines, only 10 were deemed acceptable based on the aforementioned criteria, and all have secure detections in all of the lines.

The resulting 10 targets present an exemplary sample of the galaxies in the SINS survey. They span the range in stellar mass from 0.77 to $31.6 \times 10^{10} M_\odot$, and SFR from 25 to $340 M_\odot \text{ yr}^{-1}$. They include various kinematic types, including rotation and dispersion dominated objects, as well as merging systems. For all the targets, the H α and [N II] data had already been taken during previous SINFONI observing runs. We note that two of the SINS targets from our sample (Deep3a-15504 and K20-ID5) have evidence for an AGN from X-ray, UV, and/or mid-IR data (Förster Schreiber et al. 2009; Förster Schreiber et al. 2013).

Table 1 lists all observing runs during which the data of the 10 sources with secure H α , [N II], [O III], and H β detections were obtained (observing details for other sources with only H α +[N II] data can be found in Förster Schreiber et al. 2009). The table also gives the band/grating, pixel scale, observing mode, and the total on-source integration time. For simplicity “125” refers to the largest scale with nominal pixels of $0''.125 \times 0''.250$ and field of view of $8'' \times 8''$, and “50” refers to the intermediate scale with nominal pixels of $0''.05 \times 0''.125$ and a field of view of $3''.2 \times 3''.2$.

For the data reduction, we used the software package SPRED and custom routines for optimizing the background/OH airglow subtraction. The point-spread function (PSF) full width at half maximum was measured by fitting a 2D Gaussian profile to the combined images of the PSF calibration star taken throughout the observations of a galaxy. More information on the specifics of the data reduction can be found in Förster Schreiber et al. (2009), Mancini et al. (2011), and N. M. Förster Schreiber et al. (2013, in preparation).

Table 1
Observation Details for SINS/zC-SINF Targets

Object	Band	Scale (mas)	Mode	t_{int} (s)	Observing Date(s) (MonthYY)
Q1307-BM1163	<i>J</i>	125	seeing-limited	7200	Mar05
	<i>H</i>	125	seeing-limited	14400	Mar05
Q2343-BX389	<i>H</i>	125	seeing-limited	15900	Jun06, Aug06
	<i>K</i>	125	seeing-limited	14400	Oct05
	<i>K</i>	50	LGS-AO	18000	Sep12, Oct12
Q2343-BX610 ^a	<i>H</i>	125	seeing-limited	30000	Oct05, Nov07
	<i>K</i>	125	seeing-limited	10800	Jun05, Aug05
	<i>K</i>	50	LGS-AO	30000	Sep11, Oct11, Aug12
Deep3a-6004 ^a	<i>H</i>	125	seeing-limited	13200	Feb10, Mar10
	<i>K</i>	125	seeing-limited	36000	Mar06, Mar07
	<i>K</i>	50	LGS-AO	19200	Jan10, Mar10, Jan11, Mar11, Mar12, Apr13
Deep3a-15504 ^b	<i>H</i>	125	seeing-limited	14400	Apr06
	<i>K</i>	125	seeing-limited	21600	Mar06
	<i>K</i>	50	LGS-AO	82800	Mar06–Apr11
ZC-407302	<i>H</i>	125	seeing-limited	20400	Dec09, Jan10
	<i>K</i>	125	seeing-limited	7200	Mar07
	<i>K</i>	50	LGS-AO	68400	Apr07, Apr09, Mar12
K20-ID5 ^b	<i>H</i>	125	seeing-limited	7200	Mar05
	<i>K</i>	125	seeing-limited	9600	Mar05
K20-ID7	<i>H</i>	125	seeing-limited	24000	Jan10, Feb10
	<i>K</i>	125	seeing-limited	31200	Oct05, Nov06
SSA22a-MD41	<i>H</i>	125	seeing-limited	3600	Aug06
	<i>K</i>	125	seeing-limited	25200	Nov04, Jun05
Q1623-BX599	<i>H</i>	125	seeing-limited	12000	Apr11, Jul11
	<i>K</i>	125	seeing-limited	5400	Jul04
	<i>K</i>	50	AO	7200	Apr10

Notes.

^a Has evidence for an AGN based only on spatially resolved line ratios.

^b Has evidence for an AGN from X-ray, UV, and/or mid-IR data.

2.2. Source Selection, Observations, and Data Reduction of LUCI Galaxies

We also include 12 galaxies observed with the LUCI1 NIR camera and spectrograph on the Large Binocular Telescope (Ageorges et al. 2010; Seifert et al. 2010). LUCI1 allows multi-object spectroscopy with up to 23 laser-cut masks allowing arbitrarily placed and oriented slits having widths down to $0''.1$ within a $2.5 \times 4'$ field (Buschkamp et al. 2010). These galaxies were observed in the *H*- and *K*-bands for a median integration time of 4 hr each, employing $1''$ -wide slits. With this slit width and medium resolution gratings, the spectral resolution is 2850 in the *H*-band and 2900 or 1900 in the *K*-band. The observations were taken between 2009 December and 2012 May, with seeing conditions ranging between $0''.6$ and $1''.1$. For further description of the LUCI1 instrument and the observations, see Buschkamp et al. (2010) and J. Kurk et al. (2013, in preparation).

The majority of LUCI star-forming targets were selected from the GOODS-N field based on the PEP multiwavelength catalog (Berta et al. 2011) with spectroscopic redshifts from Barger et al. (2008). In addition, galaxies were selected from the Q2343 field (Steidel et al. 2004) based on the rest-UV selected sample presented in Erb et al. (2006b). Objects from both fields were selected based on their optical redshifts such that there was minimal overlap of the $H\alpha$, [N II], [O III], and $H\beta$ emission lines with OH sky features.

The data were reduced using a custom pipeline developed at MPE (J. Kurk et al. 2013, in preparation). The pipeline

includes cosmic ray removal, correction for distortion, and the same routine to remove OH sky features as used for the SINFONI reduction (Davies 2007). The background is subtracted from frames in pairs obtained from on-slit dithering. Wavelength calibration was conducted using OH sky lines, and flux calibration using a Telluric standard star. The noise spectrum was determined using the same method as for the SINFONI data (Förster Schreiber et al. 2009).

2.3. Galaxy Properties for the Total Sample

Our total sample of 22 galaxies contains 10 SFGs from the SINS/zC-SINF survey with all four emission lines detected, 6 galaxies from the LUCI survey with all four lines detected, and 6 galaxies from the LUCI survey with an upper limit for either the [N II] or [O III] emission line and secure detections for the remaining three lines. These galaxies sample the $z \sim 1.5$ – 2.5 “main sequence” of SFGs in the stellar mass/SFR plane between stellar masses of 1×10^9 and $3 \times 10^{11} M_{\odot}$ and SFRs between 6 and $340 M_{\odot} \text{yr}^{-1}$ (Figure 1).

For the SINS/zC-SINF galaxies, stellar masses and SFRs were determined from stellar population synthesis modeling of broad-band photometry in Förster Schreiber et al. (2009), Mancini et al. (2011), and Förster Schreiber et al. (2011a), and assume either a constant star-formation history or an exponentially declining model with Bruzual & Charlot (2003) stellar evolution tracks, an Chabrier (2003) IMF, and a Calzetti et al. (2000) dust law. For Q1307-BM1163, photometry is only available in three optical bands, preventing reliable spectral energy distribution (SED) modeling to derive the stellar properties.

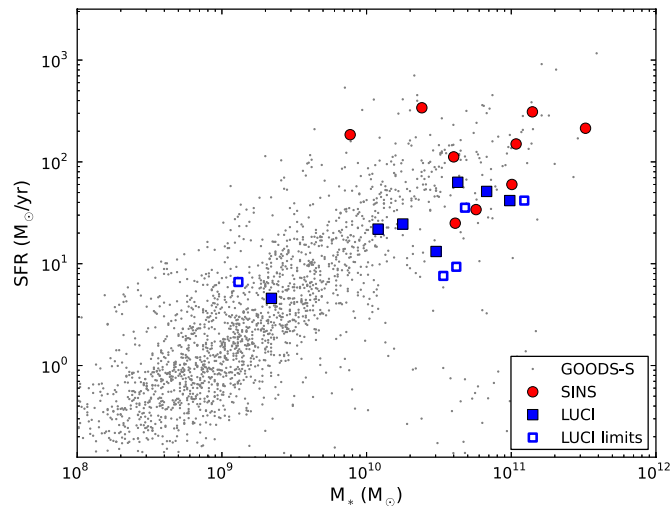


Figure 1. Location of our sample on the SFR- M_* plane. GOODS-S galaxies from $z = 1.4$ – 3 are shown as gray points (see Wuyts et al. 2012), red circles are SINS galaxies, and blue squares are LUCI galaxies. For the LUCI galaxies, we show objects that have secure detections in all four emission lines with closed symbols and those that have an upper limit in one as open symbols.

(A color version of this figure is available in the online journal.)

Galaxy properties for the LUCI sample were derived by Wuyts et al. (2011) based on broad-band SEDs. Stellar masses and SFRs are computed with the FAST routine (Kriek et al. 2009) using Bruzual & Charlot (2003) stellar evolution models with exponentially declining star-formation histories. These galaxy properties are listed in Table 2.

2.4. Extraction of Emission Line Fluxes and Maps

We extracted source- and region-integrated emission line fluxes as well as emission line maps from the final SINFONI science data cubes using line profile fitting. Prior to fitting, we applied a 3 pixel wide median filter to the data cubes to increase the signal-to-noise ratio (S/N). We then used the Gaussian fitting routine LINEFIT (Davies et al. 2011) to produce $H\alpha$ emission line flux, velocity, and velocity dispersion maps. Using these $H\alpha$ kinematic maps, we velocity-shifted all of the data cubes for each object such that the $H\alpha$ line falls at the same wavelength for each pixel in order to remove the line-broadening effect of large scale velocity gradients. We then summed the spectra of the individual pixels from the velocity-shifted cubes to obtain co-added spectra. For those galaxies that have high enough S/N data to create kinematic maps for [O III] in addition to $H\alpha$, we find that the kinematics of these lines are roughly consistent, such that we are justified in using the kinematic maps of $H\alpha$ to correct for all of the data cubes. We note that the emission line ratios do not vary significantly without this velocity shifting, but this technique allows us to recover additional flux, which is especially important for some of the fainter lines.

We obtain fluxes for each emission line by simultaneously fitting a constant continuum offset and the $H\alpha$, [N II] $\lambda 6548$, 6584, and [S II] $\lambda 6717$, 6731 lines of the co-added spectra assuming identical kinematics (velocity and line width). We then fit the [O III] $\lambda 4959$, 5007 and $H\beta$ lines assuming the same kinematics as for $H\alpha$. For all lines, we assume a Gaussian shape. The errors for the line fluxes are generated from the fit uncertainties, using the noise cube produced from the reduction as input. These errors are on average greater than those obtained from 1000 Monte Carlo simulations.

Table 2
Galaxy Properties for the Total Sample

Object	SFR ($M_\odot \text{ yr}^{-1}$)	sSFR (Gyr^{-1})	M_* ($10^{11} M_\odot$)
Q1307-BM1163 ^a	57
Q2343-BX389	25	0.61	0.41
Q2343-BX610 ^b	60	0.60	1.01
Deep3a-6004 ^b	214	0.68	3.26
Deep3a-15504 ^c	150	1.38	1.08
ZC-407302	340	13.93	0.241
K20-ID5 ^c	310	10.11	1.40
K20-ID7	112	2.84	0.40
SSA22a-MD41	185	24.03	0.077
Q1623-BX599	34	0.60	0.571
GN-7573	8	0.22	0.339
GN-21496	9	0.22	0.417
GN-16564	7	5.08	0.013
GN-31720	35	0.74	0.479
GN-4126	23	0.60	0.380
Q2343-BX442	42	0.34	1.230
GN-2602	63	1.48	0.427
GN-3493	51	0.76	0.676
GN-4104	8	1.45	0.056
GN-28625	17	1.20	0.138
GN-12976	6	2.57	0.023
Q2343-BX436	54	11.75	0.046

Notes.

^a This galaxy does not have reliable photometry, and the SFR is thus derived from $H\alpha$.

^b Has evidence for an AGN based only on spatially resolved line ratios.

^c Has evidence for an AGN from X-ray, UV, and/or mid-IR data.

In order to compare region-integrated spectra or emission line maps (for pixel-to-pixel analysis) that were derived from different bands, we used the 250 mas data cube for both, even when a 100 mas cube was available, for resolution consistency. However, we note that for the integrated spectra, we used the higher quality (from longer t_{int}) 100 mas cubes when available. For comparing emission lines from different data cubes, we register the position of the galaxy in each cube using the centroid of the continuum emission, if possible. If there is not a clear continuum signature free from residuals, we use the centroid of the $H\alpha$ and [O III] emission line fluxes, checking that the morphology and peak of emission is similar for these lines. We also find that the PSFs for different bands are consistent within 30%, which is the combined uncertainty of the resolution of the data sets. For the pixel-to-pixel analysis, we only consider pixels with a S/N of the line flux > 3 for all four emission lines.

For the LUCI targets, we collapsed the 2D data onto a 1D spectrum with an aperture chosen to optimize the S/N. We attempted a similar velocity-shifting technique as for the SINFONI data, but for the few objects for which this was possible, the procedure only increased contamination from OH features. Thus we have not used any velocity-shifted LUCI spectra, and note that as mentioned before this should not have a large effect on the emission line ratios.

The emission line fluxes for the LUCI spectra were fit using the LINEFIT routine, with errors derived from 100 Monte Carlo simulations. For lines that were undetected, a 3σ upper limit was derived based on the noise spectrum for the wavelengths corresponding to the line of interest based on the $H\alpha$ -derived redshift, assuming the same line width as $H\alpha$. For two of the galaxies from the LUCI sample (GN2602,

Table 3
Emission Line Ratios

Object	[N II]/H α	[O III] λ 5007/H β	Z/Z $_{\odot}$ (N2) ^a	Z/Z $_{\odot}$ (O3N2) ^a
Q1307-BM1163	0.256 \pm 0.024	2.29 \pm 0.16	0.75	0.45
Q2343-BX389	0.180 \pm 0.027	7.04 \pm 1.91	0.61	0.34
Q2343-BX610 ^b	0.339 \pm 0.029	1.69 \pm 0.22	0.88	0.66
Deep3a-6004 ^b	0.419 \pm 0.227	1.62 \pm 0.30	0.99	0.71
Deep3a-15504 ^c	0.350 \pm 0.089	8.13 \pm 2.00	0.89	0.40
ZC-407302	0.223 \pm 0.015	1.80 \pm 0.18	0.69	0.56
K20-ID5 ^c	0.560 \pm 0.102	7.00 \pm 0.78	1.17	0.49
K20-ID7	0.236 \pm 0.042	2.76 \pm 0.58	0.71	0.50
SSA22a-MD41	0.100 \pm 0.038	4.09 \pm 0.71	0.44	0.33
Q1623-BX599	0.167 \pm 0.030	6.48 \pm 1.33	0.58	0.34
GN-7573	0.247 \pm 0.040	4.17 \pm 0.69	0.73	0.44
GN-21496	0.204 \pm 0.034	2.53 \pm 0.70	0.66	0.49
GN-16564	0.067 \pm 0.055	7.13 \pm 2.184	0.35	0.25
GN-31720	0.162 \pm 0.060	2.97 \pm 0.86	0.58	0.43
GN-4126	0.626 \pm 0.047	7.10 \pm 2.28	1.24	0.50
Q2343-BX442	0.232 \pm 0.076	0.56 \pm 0.10	0.71	0.83
GN-2602	0.402 \pm 0.066	> 1.573 \pm 0.72	0.96	0.71
GN-3493	0.143 \pm 0.043	> 1.028 \pm 0.79	0.54	0.58
GN-4104	< 0.109 \pm 0.109	6.92 \pm 0.65	0.46	0.29
GN-28625	< 0.119 \pm 0.119	6.30 \pm 1.04	0.48	0.31
GN-12976	< 0.306 \pm 0.208	5.76 \pm 3.50	0.83	0.43
Q2343-BX436	< 0.151 \pm 0.151	4.73 \pm 0.65	0.55	0.36

Notes.

^a Assuming $Z_{\odot} = 8.69$ (Asplund et al. 2009) and using the calibration of Pettini & Pagel (2004).

^b Has evidence for an AGN based only on spatially resolved line ratios.

^c Has evidence for an AGN from X-ray, UV, and/or mid-IR data.

GN3493), the [O III] λ 5007 line was out of the range of the filter and thus the [O III] upper limit was determined from the [O III] λ 4959 emission line and adopting the approximate scaling [O III] λ 5007 = 3 \times [O III] λ 4959. In another one of our objects (GN4126) the [O III] and H β fluxes were derived from an *HST*/WFC3 Grism spectrum (B. Weiner 2013, private communication), because neither of these lines were detected in our LUCI data. These fluxes were determined using the same method as for the SINFONI spectra, except the line positions and widths were allowed to differ from those of H α because the GRISM line width is more sensitive to the object size than kinematics (the GRISM spectra are slit-less and very low resolution). Table 3 lists the [N II] λ 6584/H α and [O III] λ 5007/H β line ratios and the inferred abundances based on the N2 and O3N2 calibrations from Pettini & Pagel (2004) for our sources.

Galaxy-averaged spectra are shown for the SINS galaxies in Figure 2 and for the LUCI galaxies in Figures 3 and 4 (the latter of which contains galaxies with an upper limit for one of the lines).

3. RESULTS

3.1. Excitation Properties of $z \sim 2$ Galaxies

3.1.1. Galaxy-integrated Measurements

We show the galaxy-integrated line ratios in the BPT diagram in Figure 5. Many of the objects in our sample are located in the “composite” region of the BPT diagram, between the star-forming and AGN branches traced out by the local SDSS galaxies, and demarcated by the Kauffmann et al. (2003) and Kewley et al. (2001) empirical and theoretical divisions between star-forming and AGN galaxies. This is consistent with most findings of other recent work for samples of galaxies selected by similar criteria (Erb et al. 2006a; Shapley et al. 2005; Liu

et al. 2008; Kriek et al. 2007; Hayashi et al. 2009; Yabe et al. 2012; Trump et al. 2013; see Figure 6). The observed offset of high- z galaxies from the local star-forming branch suggests that different physical conditions and/or chemical abundances prevail in the high- z , non-AGN actively star-forming systems compared to the bulk of local SFGs (see, e.g., the detailed discussion by Liu et al. 2008). We note that all of the galaxies that are identified as AGN either from X-ray, UV, or mid-IR data, or based on spatially-resolved, rest-frame optical data (see next section and Förster Schreiber et al. 2013), have [N II]/H $\alpha \gtrsim 0.3$ independent of whether they are located in the composite or AGN region of the diagram. However, all galaxies in the composite region are not necessarily AGN. We also compare our observations with the new theoretical model of Kewley et al. (2013a, 2013b), wherein a redshift-dependent dividing line between star-forming and AGN galaxies is introduced. At $z \sim 2.2$ where most of our galaxies live, the dividing line is very similar to the Kewley et al. (2001) division, and thus Q2343-BX610 and Deep3a-6004, which we later show to have evidence for AGNs from spatially resolved data, would not be characterized as AGN galaxies. We further examine the galaxies that fall near the composite region and how to identify galaxies with obscured AGNs using spatially resolved data in the next section.

To explore some of the trends described in Liu et al. (2008) and Brinchmann et al. (2008), we color-code galaxies in the BPT diagram by SFR, stellar mass and sSFR (Figure 7). We include all of our SINS and LUCI galaxies as well as galaxies from the literature, presented in Figure 6, with secure detections in all four emission lines. Thus this analysis includes galaxies from $z = 1$ to 2.5. As expected from the mass–metallicity relation, there is a trend of increasing stellar mass with higher [N II]/H α ratios. We also find a trend of increasing offset (mostly

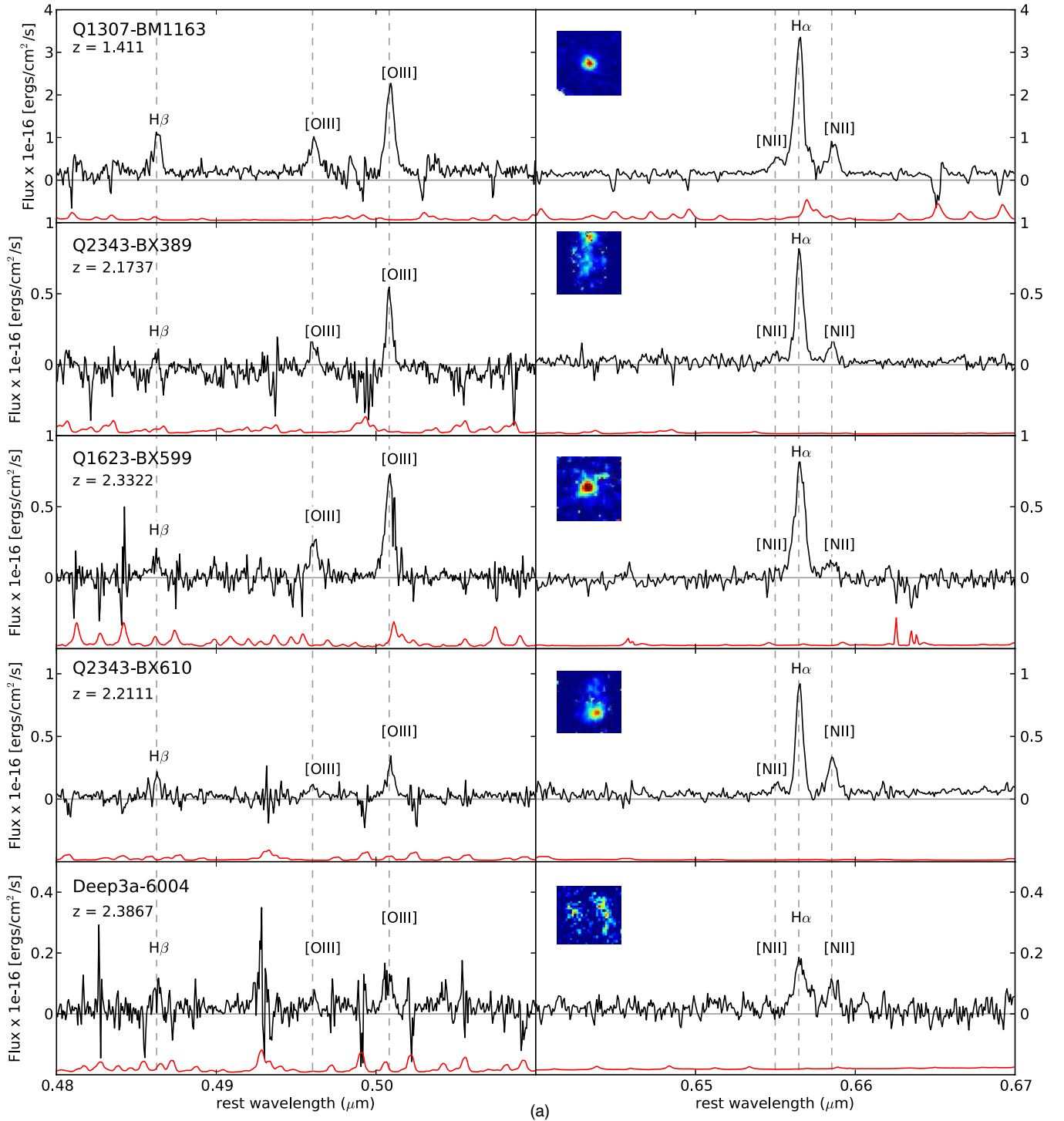


Figure 2. Galaxy spectra for five of the SINS/zC-SINF objects. The black lines show the data and the red lines show the error derived from the noise cubes. The inset in the right panels shows an AO-scale (if available) $H\alpha$ image of the galaxy.

(A color version of this figure is available in the online journal.)

in the $[N II]/H\alpha$ direction) from the $H II$ branch with increasing SFR, which may be correlated with an increase in ionization parameter, but may also be due to the aforementioned stellar mass trend, because stellar mass and SFR are tightly correlated for SFGs (Daddi et al. 2007; Rodighiero et al. 2011). Finally, there may be a (marginal) trend of increasing $[O III]/H\beta$ ratio with increasing sSFR, suggesting that galaxies in the “composite” region of the BPT diagram may be in a burstier phase of star formation than those that lie on the $H II$ branch. This is

consistent with the finding that many of the local galaxies in the “composite” region are starbursts (Liu et al. 2008; Brinchmann et al. 2008). Alternatively, the elevated sSFR for these galaxies could be related to the AGN activity affecting the line ratio, if there is a correlation between sSFR and AGN activity. However, Rangel et al. (2013) suggest that there is no such correlation.

The measured $H\beta$ fluxes might also be biased by underlying stellar $H\beta$ absorption (Dufour et al. 1980). We therefore correct for this absorption using the best fit SED-derived star-formation

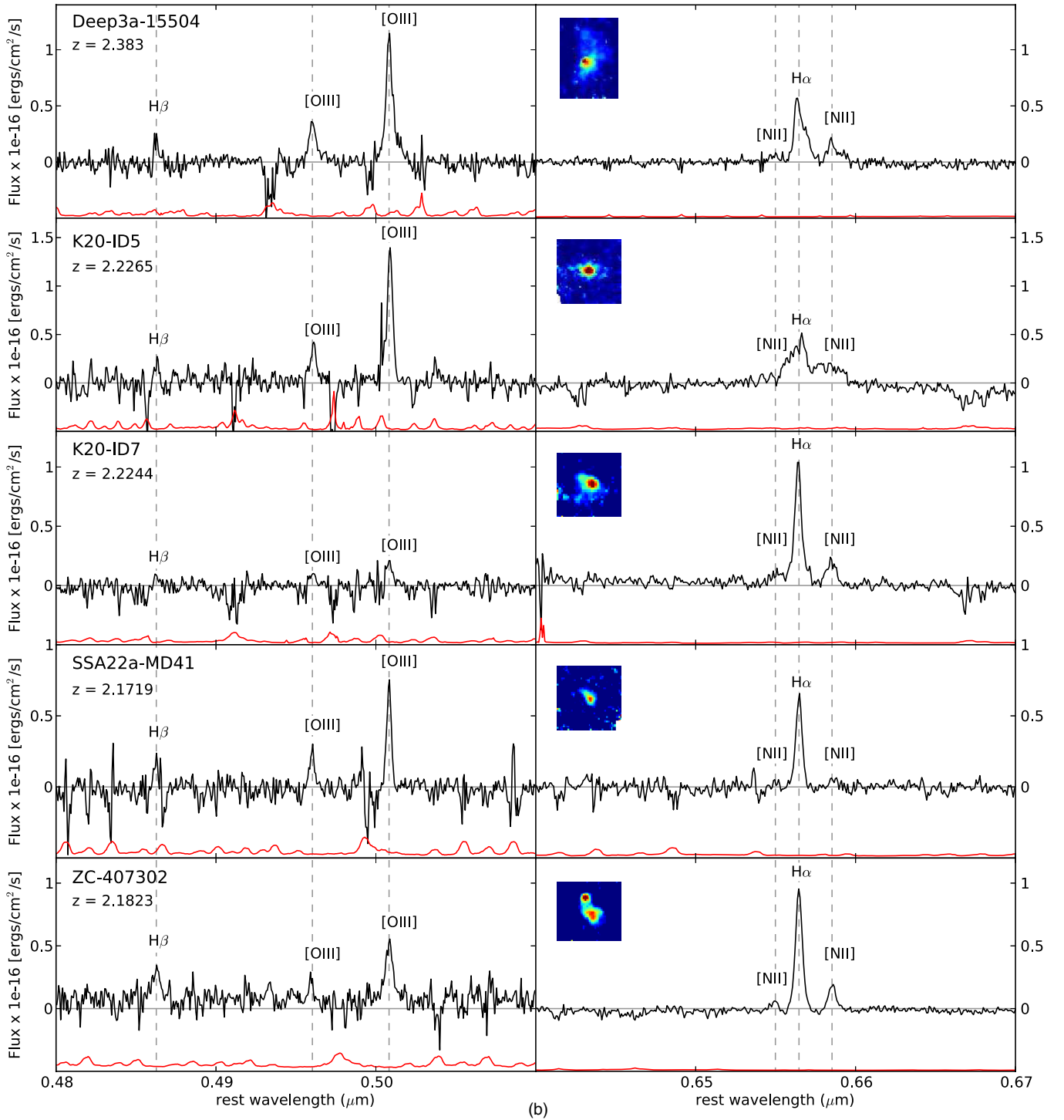


Figure 2. (Continued)

histories and ages. Once we account for this correction factor, we see a noticeable down-shift in $[O III]/H\beta$ of ~ 0.02 to 0.21 dex (mean 0.08 dex). Nevertheless, accounting for $H\beta$ absorption does not reconcile our data with the distribution of local galaxies from the SDSS (Figure 8) and therefore does not affect our qualitative conclusions. Our estimated corrections for $H\beta$ absorption are fairly similar to those of Shapley et al. (2005) who reported a maximum down-shift of 0.1 dex and also found that unaccounted for $H\beta$ absorption is likely not causing the observed offset in $[O III]/H\beta$ for their DEEP2 sample. For the remainder of this paper, we use emission line ratios that are not

corrected for stellar $H\beta$ absorption for consistency with previous work.

3.1.2. Spatially Resolved Measurements

In this section, we exploit the high-quality IFU data taken of the SINS/zC-SINF galaxies in our sample. Overall, the emission line and kinematic maps of our targets for the different emission lines are in good agreement. For most sources, the main emission peak in all of the individual line maps is found at the same location inside the source boundaries. Some notable

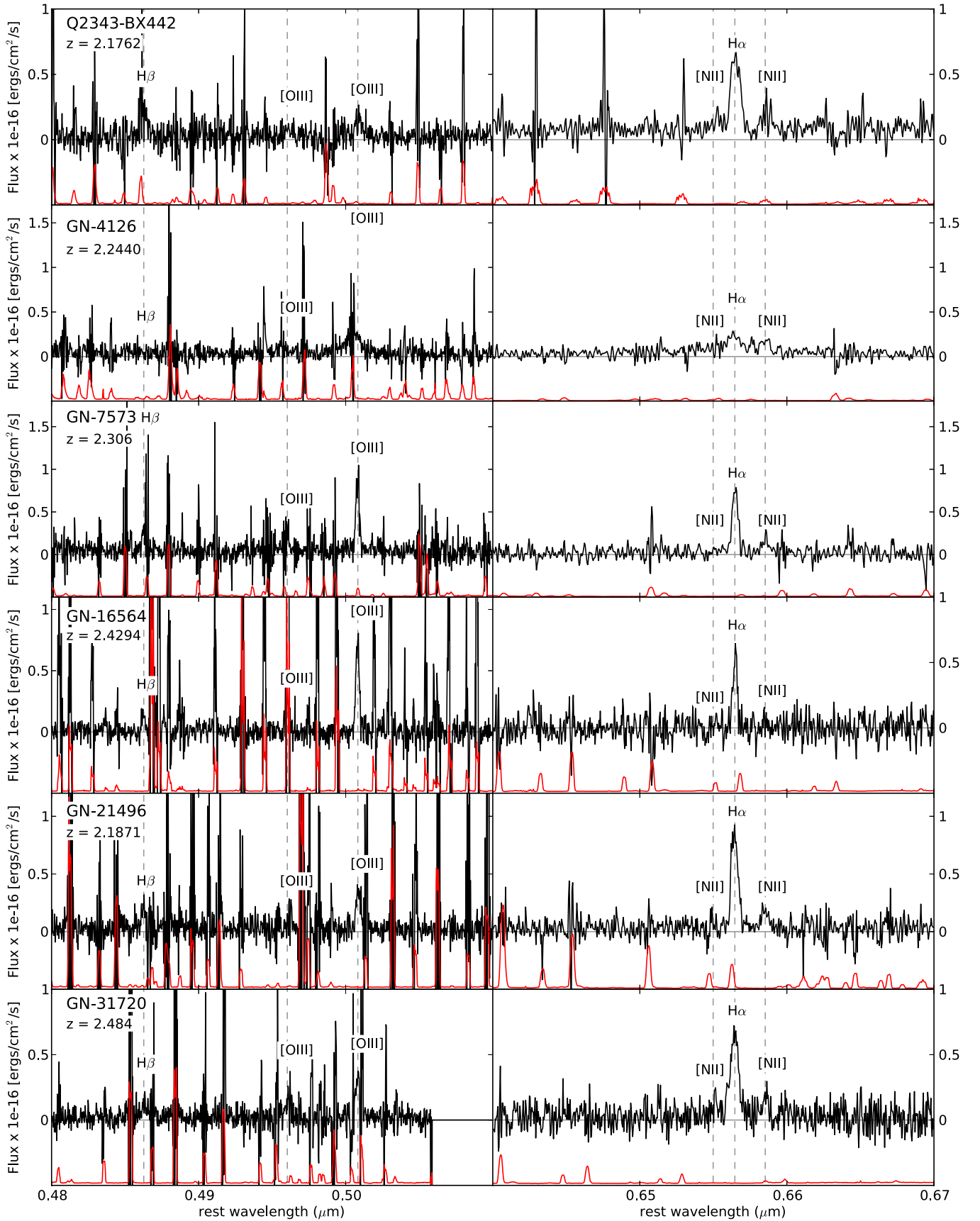


Figure 3. Galaxy spectra of LUCI galaxies with detections in all four lines. The error spectrum (red line) is shown as a factor of five lower than its actual value. (A color version of this figure is available in the online journal.)

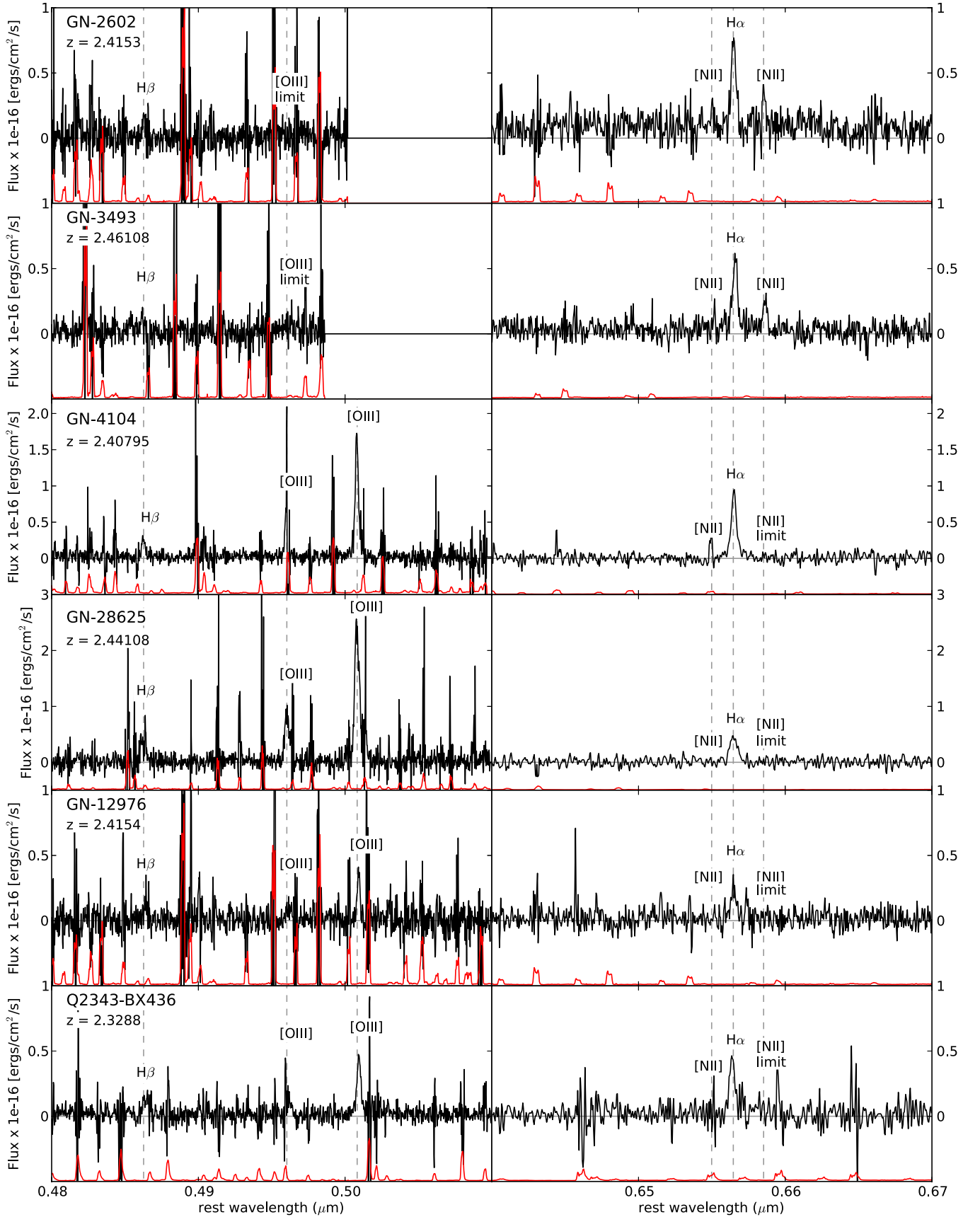


Figure 4. Galaxy spectra of LUCI galaxies with detections in three lines and an upper limit in the remaining line. For GN-2602 and GN-3493, the $[\text{O III}] \lambda 5007$ line flux was derived from $3 \times$ the $[\text{O III}] \lambda 4959$ line flux. The error spectrum (red line) is shown as a factor of five lower than its actual value.

(A color version of this figure is available in the online journal.)

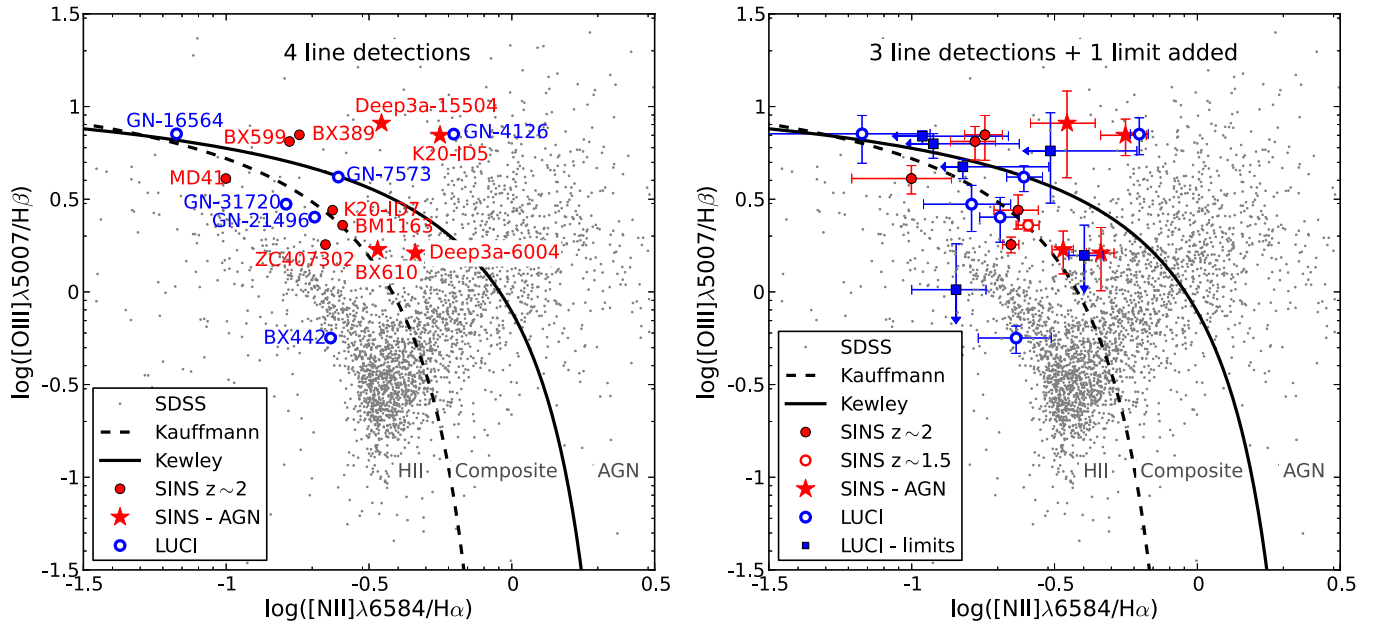


Figure 5. $[\text{N II}]/\text{H}\alpha$ vs. $[\text{O III}]/\text{H}\beta$ plane (BPT diagram). SINS galaxies are shown as either red circles (star-forming) or red stars (those identified as AGN), and LUCI galaxies are shown as blue circles, with galaxies that have only three line detections and one upper limit shown in the right panel as blue filled squares. (A color version of this figure is available in the online journal.)

exceptions exist for a couple of sources (K20-ID5 and ZC407302, see discussion later in this section), where, in particular, the peak $[\text{O III}]$ emission was somewhat offset from the $\text{H}\alpha$ peak emission. For four of the galaxies in our SINS/zC-SINF sample, the S/N is sufficiently high in all four lines ($[\text{N II}]$, $\text{H}\alpha$, $[\text{O III}]$, $\text{H}\beta$) that we are able to plot individual pixels in the BPT diagram for a large region of these galaxies. For the remaining galaxies (except Deep3a-6004), we are still able to obtain high quality spectra of the inner ($R < 0''.4$) and outer regions (see Figure 9), where the center is determined as in Section 2.

We find that many galaxies have inner regions that are offset to higher excitation relative to their outer regions, indicating that perhaps the inner region is influenced by an (possibly obscured) AGN and the outer region is dominated by star-formation (see Figure 9). Alternatively, the inner region could have a larger contribution from shock excitation or elevated ionization parameter, perhaps due to an outflow, as seen in the star-forming clumps of a $z \sim 2$ SFG presented in Newman et al. (2012). This inner/outer region offset is seen for two galaxies with strong evidence for an AGN, Deep3a-15504 and K20-ID5, as well as Q2343-BX389, which has no other evidence for an AGN (see discussion below). However, we note that the $\text{H}\beta$ line for Q2343-BX389 becomes somewhat contaminated by an OH sky line on its redshifted side, and thus its outer spectrum may be unreliable, as reflected in the error bars. For the remaining galaxies, the offsets between the inner and outer regions in the BPT diagram are consistent with the 1σ errors.

Figures 10, 11, 12, and 13 show pixel-by-pixel BPT diagrams for Deep3a-15504, ZC407302, Q1623-BX599, and Q2343-BX610 along with $[\text{N II}]/\text{H}\alpha$ and $[\text{O III}]/\text{H}\beta$ maps with a S/N cut-off of 3. There are some small discrepancies between Figure 9 and Figures 10 through 13, and these stem from the different techniques used to extract the line ratios in the pixel-by-pixel and inner/outer region analysis and the resulting flux weightings (i.e., fitting the lines to individual pixel spectra versus to integrated spectra).

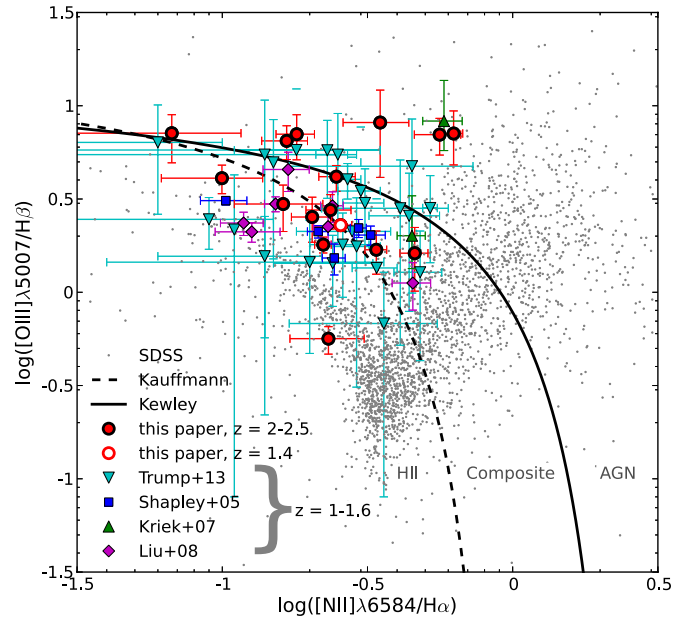


Figure 6. $[\text{N II}]/\text{H}\alpha$ vs. $[\text{O III}]/\text{H}\beta$ plane (BPT diagram). SINS and LUCI galaxies are shown as red circles, and data from Shapley et al. (2005), Kriek et al. (2007), Liu et al. (2008), and Trump et al. (2013) are blue squares, green upright triangles, magenta diamonds, and cyan inverted triangles, respectively. Only secure detections in all four lines (not upper limits) are shown. (A color version of this figure is available in the online journal.)

Deep3a-15504. Deep3a-15504 is a large, rotating massive disk which has previously been identified as an AGN based on broad and/or high excitation lines in the optical (rest-UV) spectrum (Kong et al. 2006; Genzel et al. 2006; E. Daddi 2013, private communication). In addition to elevated $[\text{N II}]/\text{H}\alpha$ values, its nuclear region also demonstrates extremely broad $\text{H}\alpha$ emission line wings, with velocities of up to 1500 km s^{-1} (Genzel et al. 2006; Förster Schreiber et al. 2013). The deep, AO-assisted $\text{H}\alpha$ map obtained for this galaxy shows that the

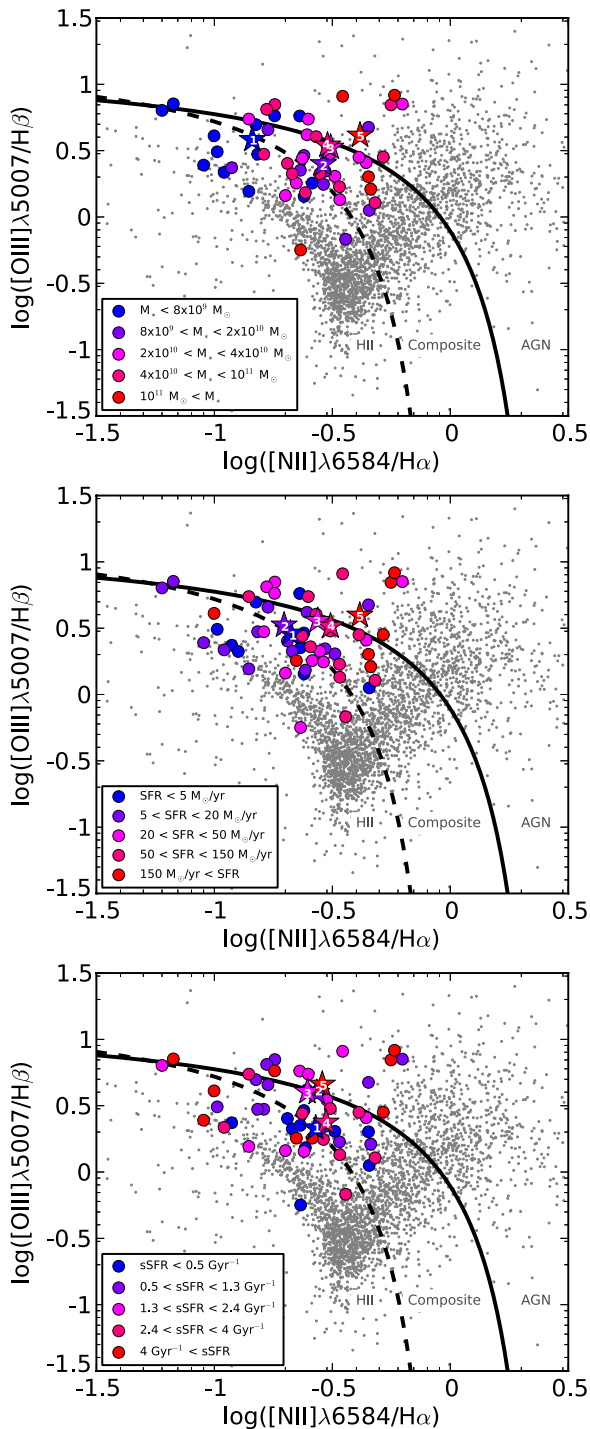


Figure 7. BPT diagram with SINS, LUCI, and literature data color-coded by M_* (top panel), SFR (middle panel), and sSFR (lower panel). Individual galaxies are shown as circles and the average of each bin is shown as a star with a number representing the order of the bin. Both M_* and SFR appear to increase with increasing $[\text{N II}]/\text{H}\alpha$, while there is perhaps a marginal trend of increasing sSFR with increasing $[\text{O III}]/\text{H}\beta$.

(A color version of this figure is available in the online journal.)

star formation activity in the large disk takes place in several moderately bright clumps superimposed on diffuse emission. With pixel-by-pixel analysis (see Figure 10), the central AGN-dominated (red and green symbols) and outer star-forming disk regions (blue pixels) separate clearly. While the outer region pixels still lie between the AGN region and the composite region of the BPT diagram, it is clear that the high excitation due

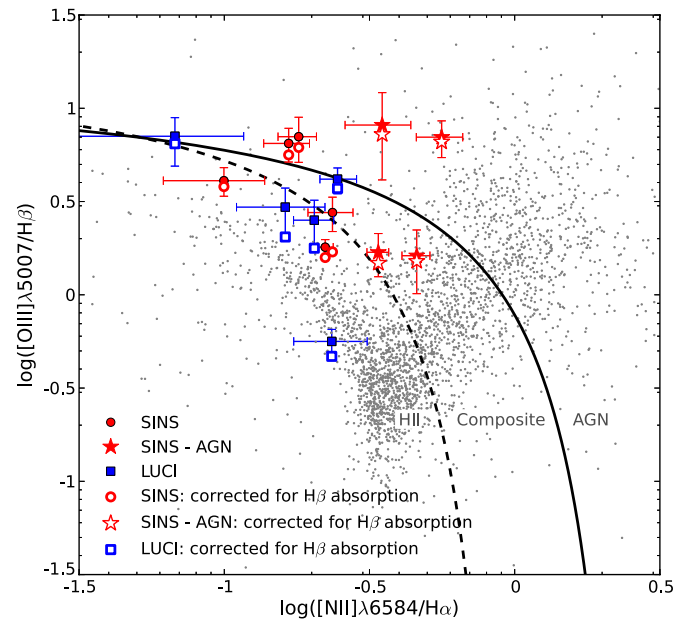


Figure 8. BPT diagram with SINS and LUCI data before (closed symbols) and after (open symbols) correction for stellar $\text{H}\beta$ absorption. The correction is marginal, with a mean offset of 0.08 dex, and cannot fully account for the elevated line ratios of $z \sim 2$ SFGs as compared with local SFGs.

(A color version of this figure is available in the online journal.)

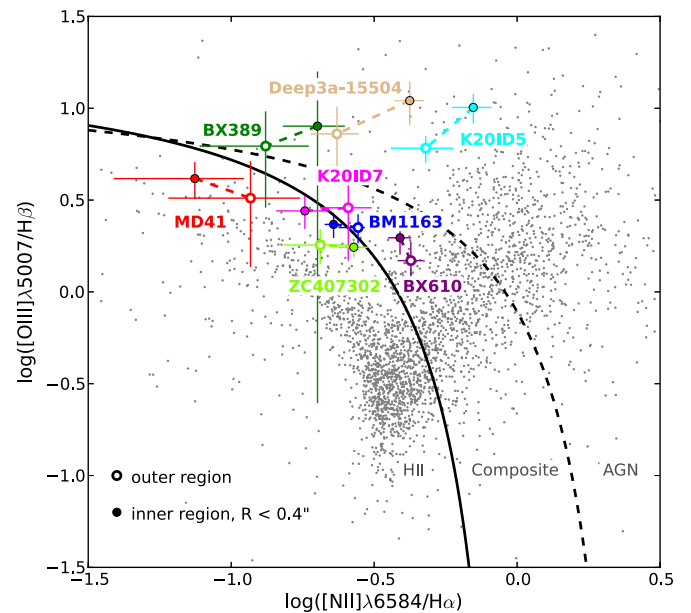


Figure 9. BPT diagram showing inner and outer regions for each galaxy. The inner regions (with $R < 0.4''$) are shown as closed symbols and the outer regions as open symbols. Several objects, particularly those in the AGN region of the diagram, show elevated line ratios in their inner regions with respect to their outer regions.

(A color version of this figure is available in the online journal.)

to the AGN at the center drives the integrated ratios to values even closer to those of the AGN regime.

ZC407302. ZC407302 has no evidence for an AGN either from resolved $\text{H}\alpha$ observations or ancillary data. This is corroborated by the pixel-by-pixel BPT diagram (Figure 11), where all pixels are consistent with excitation as observed in purely star-forming objects, and are very similar to the integrated line ratio. This is also reflected in the fairly uniform line ratio maps

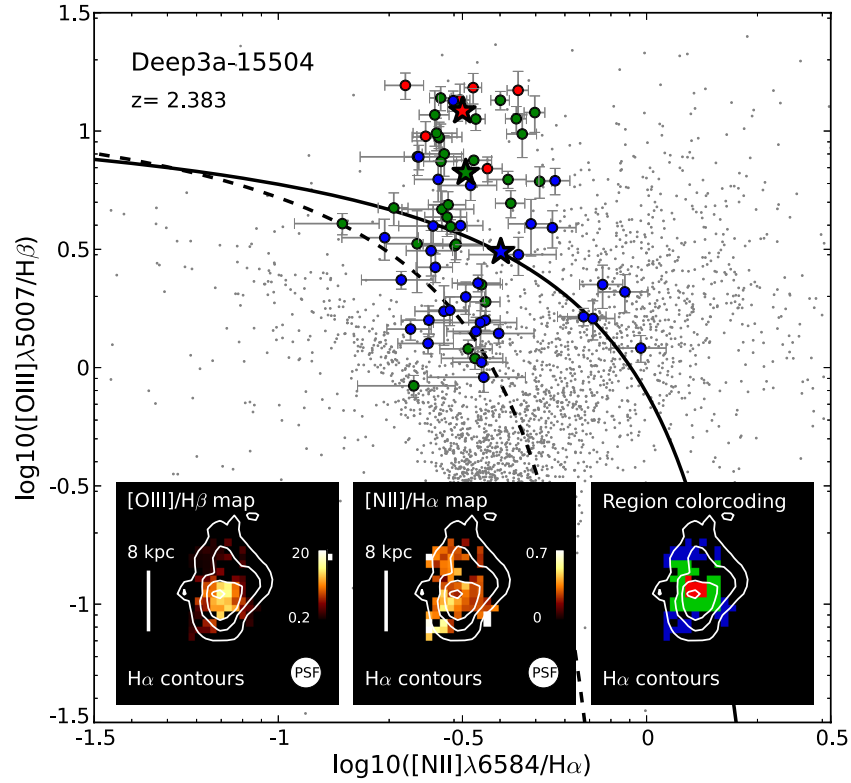


Figure 10. Pixel-by-pixel BPT diagram for Deep3a-15504. Red points are from the innermost region, green points from further out, and blue points from the furthest edges of the galaxy. The region-averaged data are shown as star symbols. The rightmost inset shows the color-coding for the regions, the middle inset shows a map of $[\text{NII}]/\text{H}\alpha$, and the left inset shows $[\text{OIII}]/\text{H}\beta$. $\text{H}\alpha$ contours appear on all three maps, and only pixels are shown with $S/N > 3$ in all four lines. The emission line maps show higher ratios in the nuclear regions, particularly for $[\text{OIII}]/\text{H}\beta$ and this is reflected in the BPT diagram. Thus, the outer region is influenced by star-formation in the disk, while the nuclear region is mostly a reflection of the AGN.

(A color version of this figure is available in the online journal.)

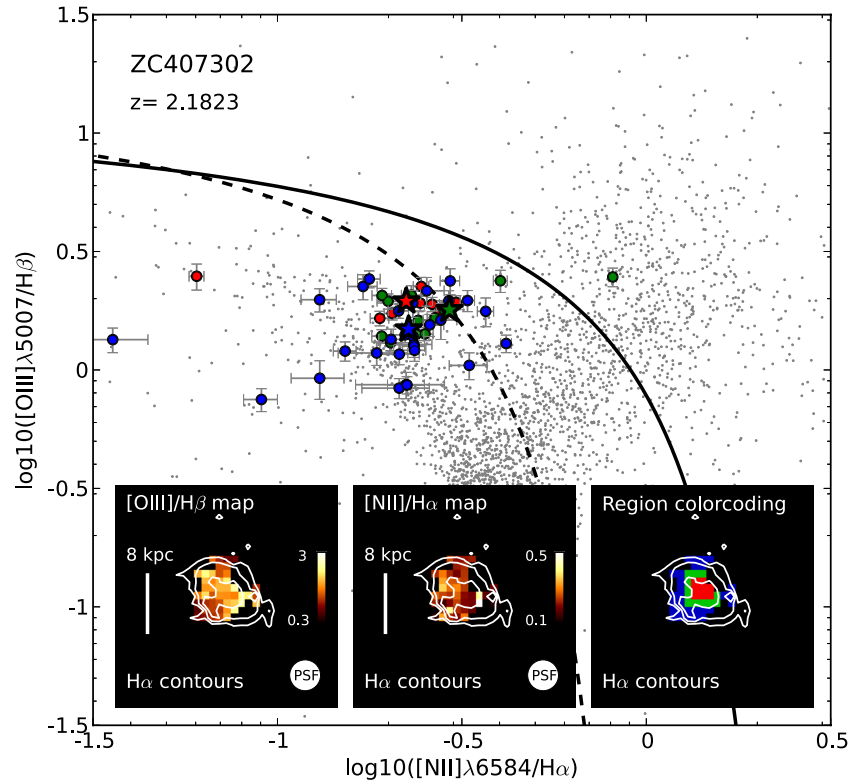


Figure 11. Pixel-by-pixel BPT diagram for ZC407302. Symbols and insets are the same as for Figure 10. The emission line ratio maps are mostly uniform and all regions of the galaxy are consistent with excitation from HII regions.

(A color version of this figure is available in the online journal.)

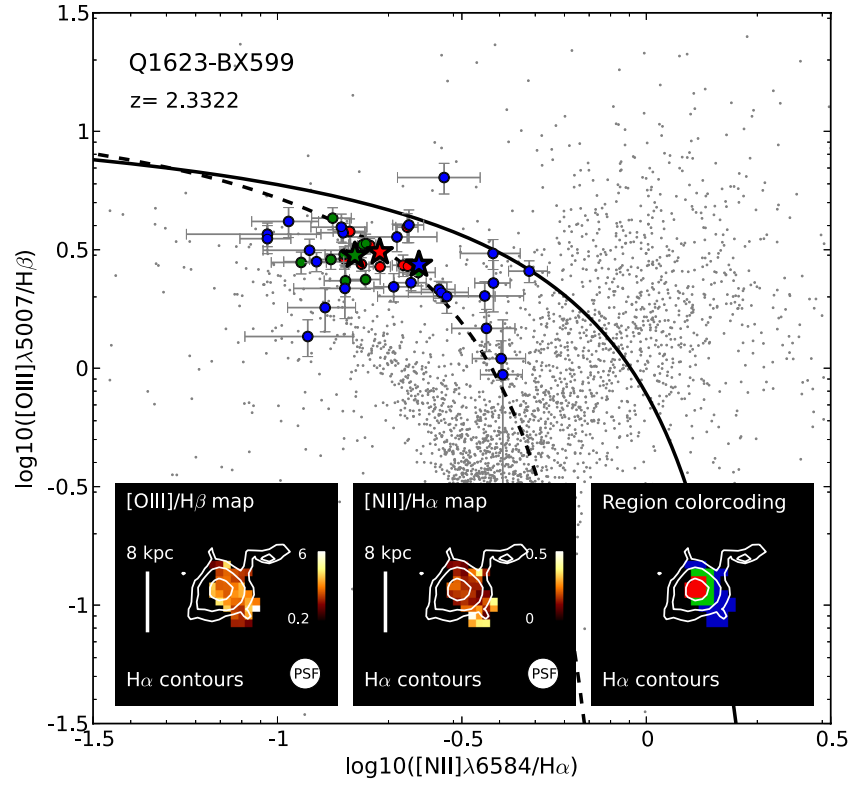


Figure 12. Pixel-by-pixel BPT diagram for Q1623-BX599. Symbols and insets are the same as for Figures 10 and 11. The emission line ratios for all regions are consistent with pure star formation.

(A color version of this figure is available in the online journal.)

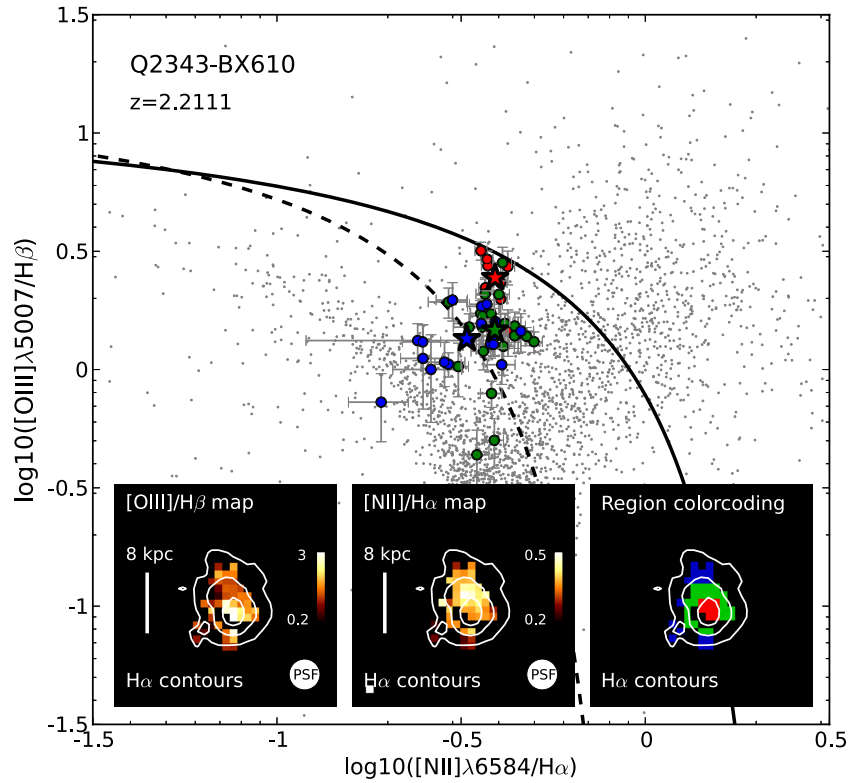


Figure 13. Pixel-by-pixel BPT diagram for Q2343-BX610. Symbols and insets are the same as for Figures 10, 11, and 12. The innermost region has elevated [N II]/H α and [O III]/H β ratios, suggestive of an AGN.

(A color version of this figure is available in the online journal.)

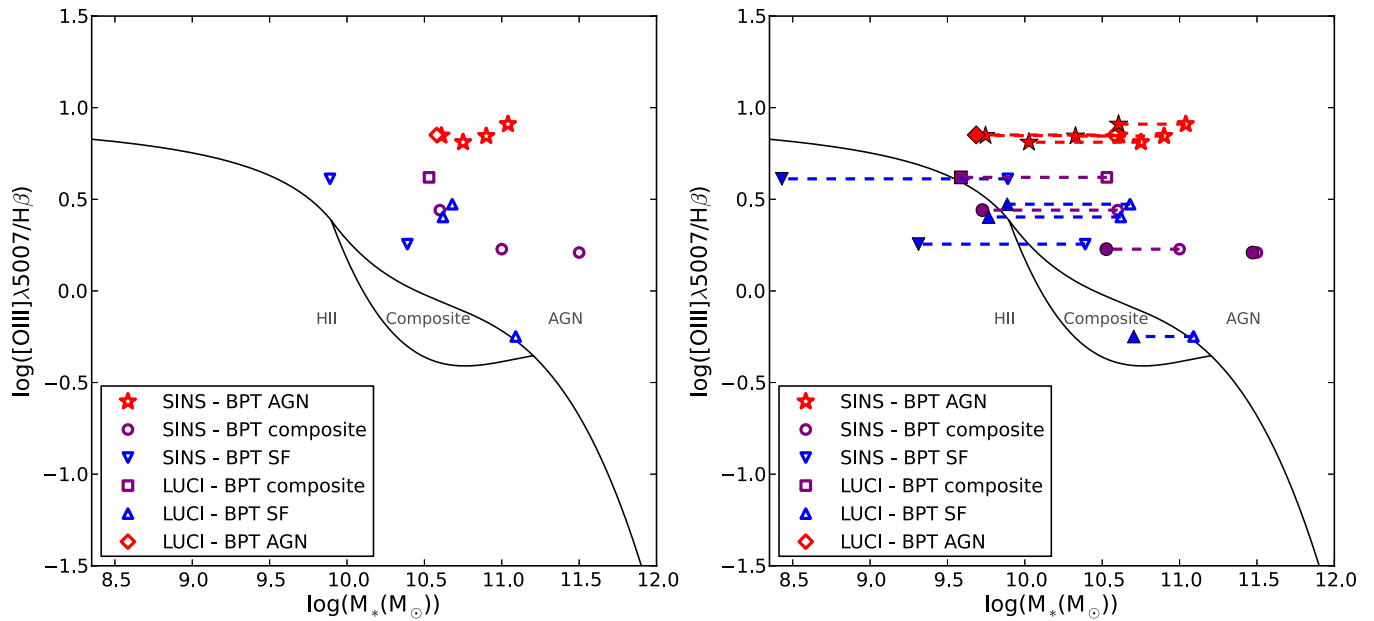


Figure 14. MEx diagnostic from Juneau et al. (2011) with SINS/zC-SINF and LUCI galaxies. The left panel shows the traditional MEx diagnostic with the galaxies’ color and symbol coded by their position in the BPT diagram. Red stars and diamonds are SINS and LUCI AGN, purple circles and squares are SINS and LUCI composite galaxies, and blue inverted and upright triangles are SINS and LUCI star-forming galaxies, according to the BPT diagram. In the right panel, we shift the data points according to the shift in the mass–metallicity relation between $z \sim 0$ and 2 (using the Erb et al. (2006a) and Tremonti et al. (2004) relations). The original points are shown as open symbols and the shifted points are shown as closed symbols. While the MEx diagnostic does not accurately predict the location of $z \sim 2$ galaxies in the BPT diagram, applying a simple shift according to the mass–metallicity relation brings the two diagnostics into better agreement. (A color version of this figure is available in the online journal.)

from the seeing-limited SINFONI data. As mentioned earlier in this section, there is a slight discrepancy between the peaks of $H\alpha$ and $[O III]$ emission. This could be due to the asymmetric light distribution in $H\alpha$ and $[N II]$ seen in the high resolution AO map (see Figure 2; Genzel et al. 2008, 2011). The asymmetry is mainly caused by a compact source northeast of the main body of the galaxy, which is not resolved in the seeing-limited maps of Figure 11, but is present in the adaptive optics data set as well as in ACS i -band and *HST* WFC3 J - and H -band imaging available for this galaxy (S. Tacchella et al., in preparation). This source could be a bright disk clump at the edge of the system or a second, lower mass galaxy interacting with the main galaxy. The overall velocity field is consistent with a large disk galaxy, while on kpc-scales, deviations from pure rotation are visible and the northeastern part appears more disturbed (Genzel et al. 2011).

Q1623-BX599. Q1623-BX599 is a compact, rotating disk (Newman et al. 2013). Like ZC407302, it has no evidence for an AGN and all three regions appear to lie in or close to the star-forming region of the BPT diagram (Figure 12). However, this galaxy does barely lie in the AGN regime of the BPT diagram based on integrated line ratios (Figure 5). This may be due to the fact that much of the east half of the galaxy has very low S/N in $H\beta$ (see $[O III]/H\beta$ map in Figure 12) and the inclusion of this region in the integrated spectrum is driving up the $[O III]/H\beta$ ratio. Based on the low $[N II]/H\alpha$ ratio for this galaxy (0.17 ± 0.03), and the results of the pixel-by-pixel analysis, it is unlikely that this galaxy harbors an AGN.

Q2343-BX610. $H\alpha$ kinematics clearly show that this system is a large rotating disk with several bright clumps visible in the AO SINFONI data as well as in high resolution NIC2 H -band and WFC3 maps (Förster Schreiber et al. 2011a, 2011b; S. Tacchella et al., in preparation). While there is no other evidence for an

AGN from the available rest-UV spectrum (Erb et al. 2006b), there is an indication of a possible AGN from the observed mid-IR IRAC colors (Hainline et al. 2012; Förster Schreiber et al. 2011a; Förster Schreiber et al. 2013) and resolved analysis of the nuclear region shows elevated emission line ratios (Figure 13, particularly in $[O III]/H\beta$) and very broad emission line wings (up to 1500 km s^{-1} ; see Förster Schreiber et al. 2013), further supporting the presence of an obscured AGN. Interestingly, while the $[O III]/H\beta$ ratio peaks in the same location as the $H\alpha$ peak, $[N II]/H\alpha$ peaks slightly north of the center, at the continuum- and kinematic-derived center (0.4 or 3.5 kpc away).

There are two additional galaxies from our sample (Deep3a-6004 and K20-ID5) that show evidence for an AGN, but do not have a sufficiently high S/N in all four lines for the pixel-by-pixel analysis. Deep3a-6004, with a ring-like $H\alpha$ morphology and kinematics suggestive of rotation (Förster Schreiber et al. 2009; Newman et al. 2013), is located in the “composite” region of the BPT diagram. While its VIMOS rest-UV spectrum shows no evidence for an AGN (E. Daddi 2013, private communication), the nuclear region has an elevated $[N II]/H\alpha$ ratio and very broad emission (up to 1500 km s^{-1} ; see Förster Schreiber et al. 2013), both suggestive of an AGN. Unfortunately, the $[O III]$ and $H\beta$ lines have too low S/N in the nuclear region to be analyzed. K20-ID5, while located in the AGN regime of the BPT diagram, has previously been characterized as a non-AGN galaxy with elevated emission line ratios due only to photoionization and shocks by van Dokkum et al. (2005). This analysis was based on the optical spectrum, which includes $[He II] \lambda 1640$ and $[C II] \lambda 1909$ emission, but no higher ionization lines such as $[C IV] \lambda 1549$ that would allow unambiguous identification of an AGN (Daddi et al. 2004). However, in recent deep 4 Ms *Chandra* observations, K20-ID5

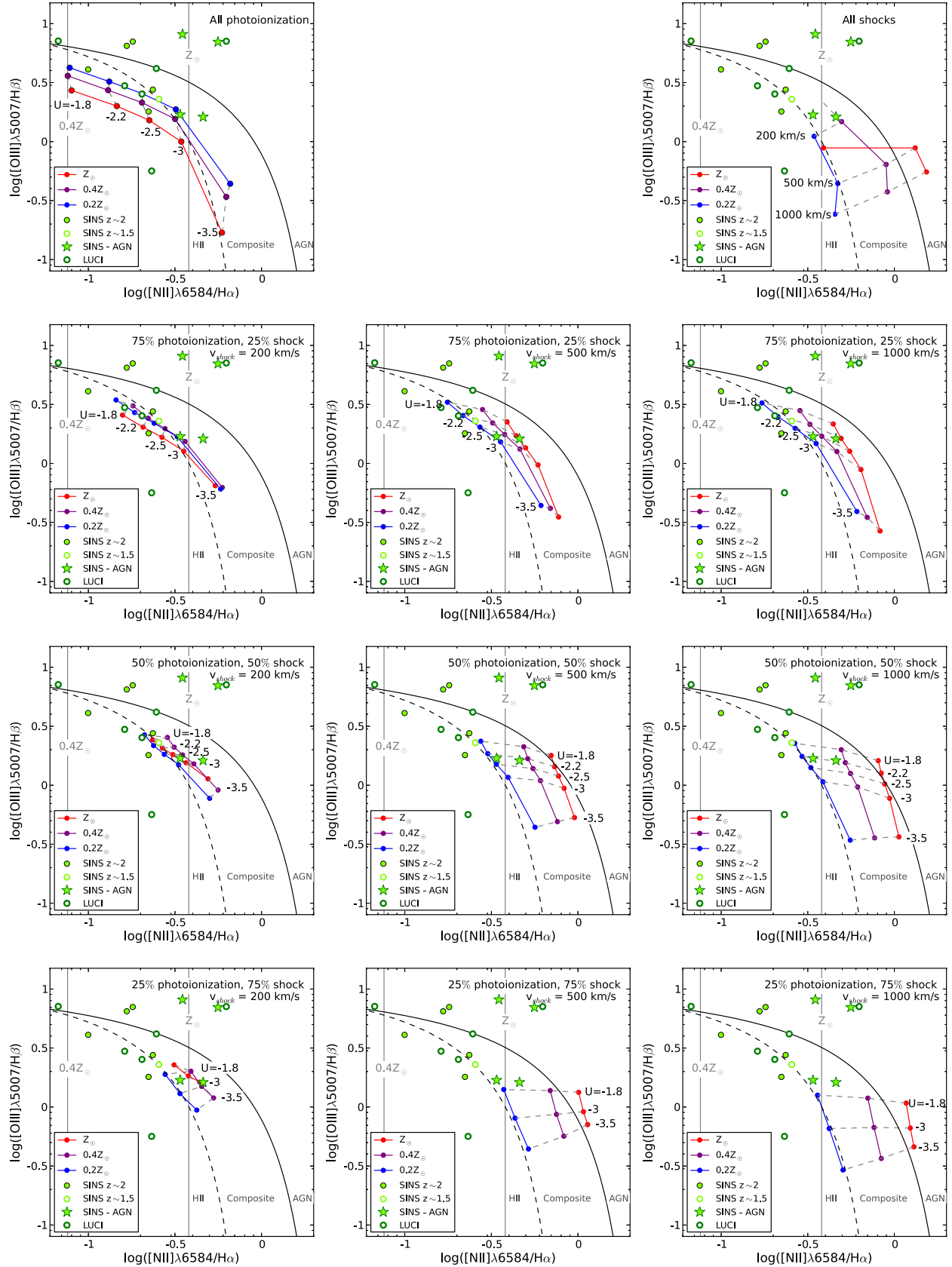


Figure 15. BPT diagram with SINS and LUCI data as well as photoionization and shock models. The different panels represent different contribution fractions from photoionization and shocks, and different shock velocities. The colored lines represent different metallicities with red, purple, and blue being Z_{\odot} , $0.4 Z_{\odot}$, and $0.2 Z_{\odot}$, respectively. The data points connected by gray dashed lines represent different ionization parameters in all but the upper right panel (where they represent different velocities), ranging from $\log U = -3.5$ to -1.8 . The vertical gray lines show the corresponding $[NII]/H\alpha$ values for Z_{\odot} and $0.4 Z_{\odot}$ using the Pettini & Pagel (2004) calibration. The combined photoionization and shock models occupy much of the “composite” region of the BPT diagram and thus these processes alone may be responsible for the positions of many $z \sim 2$ SFGs in the diagram, without the need to invoke an AGN.

(A color version of this figure is available in the online journal.)

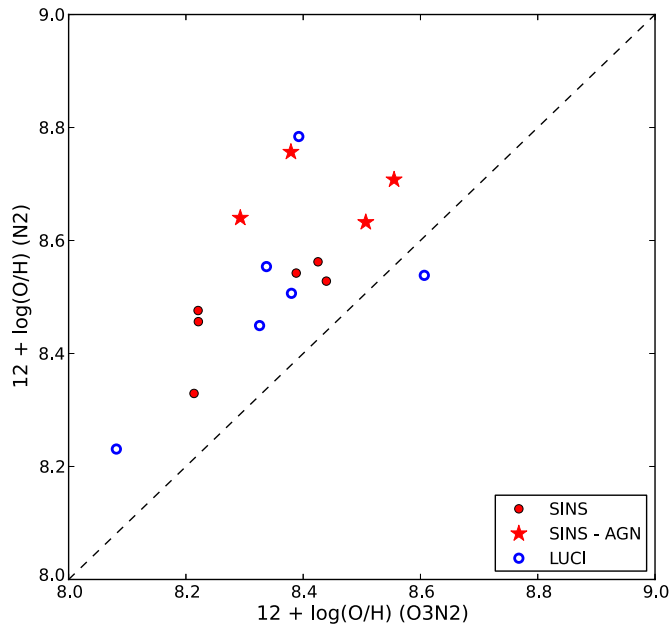


Figure 16. Comparison of gas phase metallicities calibrated using either the $[\text{N II}]/\text{H}\alpha$ calibration or the $[\text{O III}]/\text{H}\beta/[\text{N II}]/\text{H}\alpha$ calibration (both from Pettini & Pagel 2004). The 1:1 relation is shown by the dashed line, SINS galaxies are shown as red symbols (filled circles for star-forming, and stars for AGN), and LUCI galaxies are shown as blue open circles. The N2 diagnostic is biased at $z \sim 2$, systematically producing higher metallicities than the O3N2 diagnostic, even with the exclusion of AGN galaxies.

(A color version of this figure is available in the online journal.)

has been detected in both hard and soft X-rays (Xue et al. 2011), and its 1.4 GHz flux density is also consistent with the presence of an AGN. Moreover, its *Spitzer*/IRAC colors (from the catalog of Wuyts et al. 2008) also satisfy the criteria for an AGN (Stern et al. 2005; Lacy et al. 2007; Donley et al. 2012). These new data support the notion that K20-ID5 does in fact harbor an AGN, although shocks in the nucleus and the disk are not excluded.

One other galaxy from our sample (Q2343-BX389) lies in the AGN region of the BPT diagram, although it is not clear if it in fact contains an AGN. First, the $\text{H}\beta$ absorption correction brings it closer to the “composite” region of the BPT diagram (see Figure 8). Second, the $[\text{N II}]/\text{H}\alpha$ ratio (0.18 ± 0.03) is quite low for a galaxy with an AGN. Finally, the $\text{H}\beta$ line is affected by an OH sky line for a region of the galaxy and this could be affecting its positions in the BPT diagram. On the other hand, Q2343-BX389 is fairly massive ($M_* \sim 4 \times 10^{10} M_\odot$), and close to the stellar mass for which most $z \sim 2$ SFGs host an AGN ($10^{11} M_\odot$), as seen by Förster Schreiber et al. (2013), and the inner region of the galaxy is offset toward higher excitation than the outer region (Figure 9). Unfortunately, our current data are insufficient for determining whether or not this galaxy contains an AGN.

Our results from the analysis of spatially integrated line ratios, combined with other source properties, suggest that there is no single dominant mechanism common to all galaxies, which is causing the observed offset in the BPT diagram, compared to the location of local SDSS galaxies. Known AGNs (Deep3a-15504 and K20-ID5) are located in the AGN region and other sources show a similar offset as found in other high- z studies (see e.g., Erb et al. 2006a; Shapley et al. 2005; Liu et al. 2008; Kriek et al. 2007; Hayashi et al. 2009; Yabe et al. 2012; Trump et al. 2013), being located toward higher values in $[\text{N II}]/\text{H}\alpha$ and $[\text{O III}]/\text{H}\beta$

$\text{H}\beta$ and in between the AGN and star-forming branch. For these objects, contributions from (possibly low luminosity) AGNs (for Q2343-BX610 and Deep3a-6004) as well as (possibly outflow related) shocks or an ISM with higher electron density and ionization parameter (for Q1307-BM1163, K20-ID7, Q2343-BX389 and Q1623-BX599) may be possible (e.g., Shapley et al. 2005; Liu et al. 2008; Erb et al. 2006a; Wright et al. 2009, 2010; Newman et al. 2012). We probe the latter two scenarios using photoionization and shock models in Section 3.2.

We note that the effect of spatial resolution on the determination of line ratios and excitation mechanism has previously been explored by previous authors. Yuan et al. (2013a) found that coarser resolution can lead to flatter line ratio gradients and Trump et al. (2011) showed with spatially resolved WFC3 GRISM data that many low mass $z \sim 2$ SFGs could host weak AGNs, both in line with our findings.

The key result from this section is that we are able to *identify potential low-luminosity or obscured AGNs through the use of resolved line ratio measurements* (e.g., Q2343-BX610), which would not be identified as such using integrated data. Using this technique, we also find that not all high- z galaxies in or near the composite region appear to contain AGNs.

3.1.3. MEx Diagnostic at High- z

Recently, Juneau et al. (2011) introduced a new excitation diagnostic that could be used in the absence of an $[\text{N II}]$ and $\text{H}\alpha$ measurement, the Mass-Excitation (MEx) diagnostic. This diagnostic uses the well-known correlation between galaxy stellar mass and gas phase metallicity to create an alternate BPT-like diagram with $[\text{O III}]/\text{H}\beta$ versus stellar mass. While both Juneau et al. (2013) and Trump et al. (2013) have shown that this relation, which was calibrated locally, holds up to $z \lesssim 1.6$, separating AGN and SFGs, we hope to test whether this relation could also be used for our $z \sim 2$ objects.

As seen in the left panel of Figure 14, we find that this diagnostic does not work for our $z \sim 2$ galaxies. All of our galaxies with all four emission lines ($[\text{N II}]$, $\text{H}\alpha$, $[\text{O III}]$, $\text{H}\beta$) fall in the AGN regime of the MEx diagram regardless of their position in the original BPT diagram. This is not surprising given the strong offset of $z \sim 2$ galaxies in the stellar mass–metallicity relation. In order to quantify the effect of the evolution of the mass–metallicity relation on this discrepancy, we derive a simple correction for the stellar mass (i.e., what would the stellar mass of our $z \sim 2$ galaxies be at $z \sim 0$ for the same value of $[\text{N II}]/\text{H}\alpha$). First, we calculate the shift in stellar mass as a function of metallicity between the Erb et al. (2006a) $z \sim 2$ relation and the Tremonti et al. (2004) SDSS local relation (using the N2 indicator). Then we use the Erb et al. (2006b) mass–metallicity relation to get the mass shift as a function of stellar mass and apply this shift to our $z \sim 2$ galaxies in Figure 14 (right panel). We note that this correction cannot account for the presence of shocks and elevated ionization parameter, which could also affect the MEx diagnostic at $z \sim 2$.

We find that this corrected MEx diagnostic does a reasonably good job of predicting the location of the galaxies in the BPT diagram: The BPT SFGs (left of the Kauffmann et al. (2003) relation) all fall in the MEx star-forming regime or close to it; all but one of the BPT composite galaxies are shifted toward the border between the AGN and star-forming regimes; and the BPT AGN galaxies are still in the MEx AGN regime. In fact, we find that the two BPT composite galaxies that still lie in the AGN regime of the “corrected” MEx diagram

(Deep3a-6004 and Q2343-BX610) are also classified as AGN when using spatially resolved analysis.

3.2. Comparison to Photoionization and Shock Models

We generate both photoionization and shock models to explore the effect of these processes on the location of high- z galaxies in the BPT diagram. The photoionization models are created using SEDs generated with Starburst99 (Leitherer et al. 1999; Vázquez & Leitherer 2005), along with the photoionization code Cloudy (Ferland et al. 2013). We assume a spherical geometry, a uniform electron density of 100 cm^{-3} , and an ISM dust model. In generating the SEDs we assume a 10 Myr old cloud with a constant SFR of $100 M_{\odot} \text{ yr}^{-1}$ (the median for the SINS galaxies), a Kroupa (2001) IMF, high mass-loss stellar evolution tracks from the Geneva group (Meynet et al. 1994), and a Pauldrach/Hillier atmosphere (Pauldrach et al. 2001; Hillier & Miller 1998). Models are generated for a range of metallicities (for $0.2 Z_{\odot}$, $0.4 Z_{\odot}$ and Z_{\odot}) and ionization parameters ($\log U = -3.5$ to -1.8). Using an open geometry has little effect on the resulting line ratios, as does altering the filling factor (we consider a filling factor of one here), changing the density (between 1 and 500 cm^{-3}), adding molecules, removing the grain model, or changing the SFR by an order of magnitude.

The shock models are generated according to the method outlined in Gnat & Sternberg (2009) for the same metallicities as above (0.2 – $1 Z_{\odot}$) and for shock velocities of 200, 500, and 1000 km s^{-1} (comparable to the velocities of the warm ionized component and hot wind fluid in galactic outflows, see Veilleux et al. 2005; Genzel et al. 2011). In these shock models, we have calculated the non-equilibrium ionization and cooling, followed the radiative transfer of the shock self-radiation through the postshock cooling layers, taken into account the resulting photoionization and heating, and followed the dynamics of the cooling gas. We have also followed the emission-line intensities of several lines produced in the postshock cooling layers.

To obtain models with both photoionization and shocks, we normalize the lines fluxes in each of the photoionization and shock models by the $H\alpha$ flux, and combine them with varying contributions, as shown in Figure 15. The SINS and LUCI data (particularly in the “composite” region of the BPT diagram) are best fit by the models with a 25% flux contribution to the $H\alpha$ emission from shocks, and are fit equally well with either the 500 or 1000 km s^{-1} shock velocity models, or the 200 km s^{-1} model with a 50%–75% flux contribution from shocks. Incidentally, this is consistent with what was found by Newman et al. (2012) for the fraction of $H\alpha$ emission deriving from shocks (15%–30%) in winds from individual star-forming clumps in a $z \sim 2$ SFG, assuming the higher velocity models. However, we note that if the $H\beta$ absorption correction shown in Figure 8 is applied, the data points may be more consistent with the 100% photoionization model. Both the 100% and the 75% photoionization models imply ionization parameters of $\log U = -3$ to -1.8 for our galaxies.

If we compare the metallicities from the models with those assumed using the Pettini & Pagel (2004) $[\text{N II}]/H\alpha$ calibration (indicated by the gray lines in Figure 15), we find that galaxies determined to have close to solar metallicity based solely on their $[\text{N II}]/H\alpha$ ratios could indeed have metallicities as low as $0.2 Z_{\odot}$ when accounting for photoionization effects and shocks (for both galaxies with and without evidence for AGNs). The discrepancy is lower when the metallicities are calibrated using the O3N2 diagnostic (see next section, and Table 3), but there is still a significant offset between that calibration and the

metallicities determined from the models. When considering the non-AGN galaxies that fall within the best fit model grid (Q1307-BM1163, K20-ID7, GN-21496), the metallicities (Z/Z_{\odot}) calculated with the N2 diagnostic are overestimated (as compared with the models) by a factor of ~ 3 , and those calculated with the O3N2 diagnostic are overestimated by a factor of ~ 2 .

Our models are roughly consistent with those of previous work on photoionization and shock models (see e.g., Dopita & Sutherland 1995; Dopita et al. 2000, 2006; Allen et al. 2008; Levesque et al. 2010; Rich et al. 2011). The 100% photoionization models occupy a similar region of parameter space (mostly in the H II region and part of the composite region), as those from Dopita et al. (2000, 2006), and Levesque et al. (2010), and the shock model produces similar line intensities as for other fast shock codes (e.g., Allen et al. 2008). We compare our combined shock and photoionization models to those of Rich et al. (2011), and find good overall agreement, with $[\text{N II}]/H\alpha$ increasing with shock fraction, although we find an overall decrease in $[\text{O III}]/H\beta$ with shock fraction while they find an increase.

From our models, we find that most or all of the galaxies located in the “composite” region of the BPT diagram need not contain an AGN and may only lie there because of shocks and photoionization (particularly if we correct $H\beta$ for stellar absorption). Rich et al. (2010, 2011) showed a similar effect of shocks on local galaxies in the BPT diagram. Furthermore, metallicities based solely on the $[\text{N II}]/H\alpha$ local calibration could be severely overestimated, and these models allow us to determine the expected metallicities when shocks are present.

3.3. Comparison of Metallicity Indicators

A discussion of the mass–metallicity relation for the full SINS/zC-SINF and LUCI samples as well as resolved metallicity gradients will be discussed by J. Kurk et al. (2013, in preparation). Here, we compare the gas phase metallicities derived using different nebular line ratios, all calibrated locally. Kewley & Ellison (2008), among others, have shown that the choice of metallicity calibration can have a large effect on the resulting metallicity, even for local SDSS galaxies. However, here we explore additional systematic discrepancies that can arise from differing ISM conditions in high- z galaxies.

In Figure 16, we have plotted the O3N2- versus N2-based metallicities of our galaxies using the Pettini & Pagel (2004) calibrations. The deviation from the 1:1 relation is reminiscent of the offset above the SDSS star-forming sequence in the BPT diagram (Figure 5), and could reflect different physical conditions locally and at $z \sim 2$ or an obscured AGN contribution, driving the line excitation. Indeed, for AGN galaxies we find a mean offset between the gas-phase metallicities derived with the two different methods of 0.28 dex (stddev = 0.12 dex), while for the non-AGN galaxies, we find a mean offset of 0.16 dex (stddev = 0.06 dex). If we account for stellar $H\beta$ absorption, as previously shown in Figure 8 for the BPT diagram, the deviation from the 1:1 relation decreases but the average offset is still 0.13 dex (stddev = 0.06 dex) for the non-AGN and 0.24 (stddev = 0.12 dex) for the AGN galaxies, toward lower $\log(\text{O}/\text{H})$ with the O3N2 calibration.

Thus, as shown by Liu et al. (2008), some metallicity calibrations (e.g., N2) are more affected than others by the presence of shocks, AGNs, or higher interstellar pressure, and even while excluding the AGN galaxies, there is still an offset between the two calibrations. As mentioned in the previous

section, using the O3N2 calibration brings the metallicity determinations into closer agreement with the photoionization and shock models presented here (as compared with the N2 calibration), but there is still some inconsistency. Despite the observed offsets, relative measurements among galaxies remain unaltered and the use of one or the other indicator would lead to similar conclusions.

Based on our findings here and in Section 3.2, it is possible that the mass–metallicity relation at $z \sim 2$ based on the $[\text{N II}]/\text{H}\alpha$ diagnostic could be overestimated by a factor of 2–3 in Z . This discrepancy may be even worse considering that we have excluded from this calculation AGNs that have been identified solely based on spatially resolved observations.

4. CONCLUSIONS

Based on 22 $z \sim 1.4$ – 2.5 SFGs from the SINS/zC-SINF and LUCI surveys (10 with spatially resolved data), we explore the effects of AGNs, shocks, and photoionization on line-ratio diagnostics at $z \sim 2$. In particular, our spatially resolved data allow us to investigate how integrated line ratio measurements may be impacted by different excitation mechanisms. Our findings are as follows:

1. With the use of spatially resolved line ratios, we are able to identify low-luminosity or obscured AGNs that would otherwise not be detectable from integrated measurements, wherein the line ratios are the product of both a star-formation dominated disk and a highly excited nuclear region.
2. Shocks and photoionization may be responsible for the location of many $z \sim 2$ galaxies in the “composite” region of the BPT diagram. Shocks could contribute up to $\sim 25\%$ of the $\text{H}\alpha$ flux for our sample.
3. In the composite region of the BPT diagram, there is a mix of galaxies with and without evidence for AGNs and the prevalence of an AGN in this region appears to be correlated with $[\text{N II}]/\text{H}\alpha$ (or similarly M_*).
4. The MEx diagnostic (Juneau et al. 2011) does not accurately separate $z \sim 2$ star-forming and AGN galaxies according to the BPT diagram. However, applying a shift to M_* values based on the offset between the local and $z \sim 2$ mass–metallicity relations improves consistency of galaxy classification between the BPT and MEx diagrams.
5. Gas-phase metallicities that are determined from local calibrations appear biased to higher metallicities at high- z when the presence of photoionization and shocks are considered, by up to a factor of three (when using the N2 calibration) or two (when using the O3N2 calibration).

The key take-away messages from this paper are that one must be careful when using integrated line ratios, as there may be a large range in excitation that is hidden in the average spectrum and that the effects of shocks, photoionization, and the presence of an AGN may all be responsible for elevated line ratios in $z \sim 2$ SFGs.

We thank the ESO staff, especially those at Paranal Observatory, for their ongoing support during the many past and continuing observing runs over which the SINS project is being carried out, as well as the LBTO staff. We also acknowledge the SINFONI, PARSEC, and LUCI teams, whose devoted work on the instruments and lasers paved the way for the success of the SINS and LUCI observations. In addition, we thank Jonathan Trump for supplying the errors for his BPT data. S.F.N. is supported by

an NSF grfp grant. C.M., A.R., and G.Z. acknowledge partial support by the ASI grant “COFIS-Analisi Dati” and by the INAF grant “PRIN-2008” and “PRIN-2010.” O.G. was supported by program number AR12655 provided by NASA through a grant from STScI, under NASA contract NAS5-2655.

REFERENCES

- Abraham, R. G., Glazebrook, K., McCarthy, P. J., et al. 2004, *AJ*, **127**, 2455
 Adelberger, K. L., Steidel, C. C., Shapley, A. E., et al. 2004, *ApJ*, **607**, 226
 Ageorges, N., Seifert, W., Jütte, M., et al. 2010, *Proc. SPIE*, **7735**, 77351L
 Allen, M. G., Groves, B. A., Dopita, M. A., Sutherland, R. S., & Kewley, L. J. 2008, *ApJS*, **178**, 20
 Asplund, M., Grevesse, N., Sauval, A. J., & Scott, P. 2009, *ARA&A*, **47**, 481
 Baldwin, J. A., Phillips, M. M., & Terlevich, R. 1981, *PASP*, **93**, 5
 Barger, A. J., Cowie, L. L., & Wang, W.-H. 2008, *ApJ*, **689**, 687
 Berta, S., Magnelli, B., Nordon, R., et al. 2011, *A&A*, **532**, A49
 Bonzini, M., Mainieri, V., Padovani, P., et al. 2012, *ApJS*, **203**, 15
 Brinchmann, J., Pettini, M., & Charlot, S. 2008, *MNRAS*, **385**, 769
 Bruzual, G., & Charlot, S. 2003, *MNRAS*, **344**, 1000
 Buschkamp, P., Hofmann, R., Gemperlein, H., et al. 2010, *Proc. SPIE*, **7735**, 773579
 Calzetti, D., Armus, L., Bohlin, R. C., et al. 2000, *ApJ*, **533**, 682
 Chabrier, G. 2003, *PASP*, **115**, 763
 Cimatti, A., Daddi, E., Mignoli, M., et al. 2002, *A&A*, **381**, L68
 Cowie, L. L., Hu, E. M., & Songaila, A. 1995, *AJ*, **110**, 1576
 Cresci, G., Hicks, E. K. S., Genzel, R., et al. 2009, *ApJ*, **697**, 115
 Daddi, E., Cimatti, A., Renzini, A., et al. 2004, *ApJL*, **600**, L127
 Daddi, E., Dickinson, M., Morrison, G., et al. 2007, *ApJ*, **670**, 156
 Davies, R., Förster Schreiber, N. M., Cresci, G., et al. 2011, *ApJ*, **741**, 69
 Davies, R. I. 2007, *MNRAS*, **375**, 1099
 Donley, J. L., Koekemoer, A. M., Brusa, M., et al. 2012, *ApJ*, **748**, 142
 Dopita, M. A., Fischera, J., Sutherland, R. S., et al. 2006, *ApJS*, **167**, 177
 Dopita, M. A., Kewley, L. J., Heisler, C. A., & Sutherland, R. S. 2000, *ApJ*, **542**, 224
 Dopita, M. A., & Sutherland, R. S. 1995, *ApJ*, **455**, 468
 Dufour, R. J., Talbot, R. J., Jr., Jensen, E. B., & Shields, G. A. 1980, *ApJ*, **236**, 119
 Elmegreen, B. G., & Elmegreen, D. M. 2005, *ApJ*, **627**, 632
 Elmegreen, B. G., & Elmegreen, D. M. 2006, *ApJ*, **650**, 644
 Elmegreen, D. M., Elmegreen, B. G., Marcus, M. T., et al. 2009, *ApJ*, **701**, 306
 Elmegreen, D. M., Elmegreen, B. G., & Sheets, C. M. 2004, *ApJ*, **603**, 74
 Epinat, B., Contini, T., Le Fèvre, O., et al. 2009, *A&A*, **504**, 789
 Epinat, B., Tasca, L., Amram, P., et al. 2012, *A&A*, **539**, A92
 Erb, D. K., Shapley, A. E., Pettini, M., et al. 2006a, *ApJ*, **644**, 813
 Erb, D. K., Shapley, A. E., Steidel, C. C., et al. 2003, *ApJ*, **591**, 101
 Erb, D. K., Steidel, C. C., Shapley, A. E., et al. 2006b, *ApJ*, **646**, 107
 Ferland, G. J., Porter, R. L., van Hoof, P. A. M., et al. 2013, *RMxAA*, **49**, 137
 Förster Schreiber, N. M., Genzel, R., Bouché, N., et al. 2009, *ApJ*, **706**, 1364
 Förster Schreiber, N. M., Genzel, R., Lehnert, M. D., et al. 2006, *ApJ*, **645**, 1062
 Förster Schreiber, N. M., Genzel, R., Newman, S. F., et al. 2013, *arXiv:1311.2596*
 Förster Schreiber, N. M., Shapley, A. E., Erb, D. K., et al. 2011a, *ApJ*, **731**, 65
 Förster Schreiber, N. M., Shapley, A. E., Genzel, R., et al. 2011b, *ApJ*, **739**, 45
 Genzel, R., Burkert, A., Bouché, N., et al. 2008, *ApJ*, **687**, 59
 Genzel, R., Newman, S., Jones, T., et al. 2011, *ApJ*, **733**, 101
 Genzel, R., Tacconi, L. J., Eisenhauer, F., et al. 2006, *Natur*, **442**, 786
 Gnat, O., & Sternberg, A. 2009, *ApJ*, **693**, 1514
 Hainline, K. N., Shapley, A. E., Greene, J. E., et al. 2012, *ApJ*, **760**, 74
 Hayashi, M., Motohara, K., Shimasaku, K., et al. 2009, *ApJ*, **691**, 140
 Hillier, D. J., & Miller, D. L. 1998, *ApJ*, **496**, 407
 Jones, T., Ellis, R., Jullo, E., & Richard, J. 2010, *ApJL*, **725**, L176
 Jones, T., Stark, D. P., & Ellis, R. S. 2012, *ApJ*, **751**, 51
 Juneau, S., Dickinson, M., Alexander, D. M., & Salim, S. 2011, *ApJ*, **736**, 104
 Juneau, S., Dickinson, M., Bournaud, F., et al. 2013, *ApJ*, **764**, 176
 Kauffmann, G., Heckman, T. M., Tremonti, C., et al. 2003, *MNRAS*, **346**, 1055
 Kewley, L. J., Dopita, M. A., Leitherer, C., et al. 2013a, *ApJ*, **774**, 100
 Kewley, L. J., Dopita, M. A., Sutherland, R. S., Heisler, C. A., & Trevena, J. 2001, *ApJ*, **556**, 121
 Kewley, L. J., & Ellison, S. L. 2008, *ApJ*, **681**, 1183
 Kewley, L. J., Groves, B., Kauffmann, G., & Heckman, T. 2006, *MNRAS*, **372**, 961
 Kewley, L. J., Maier, C., Yabe, K., et al. 2013b, *ApJL*, **774**, L10
 Komatsu, E., Smith, K. M., Dunkley, J., et al. 2011, *ApJS*, **192**, 18
 Kong, X., Daddi, E., Arimoto, N., et al. 2006, *ApJ*, **638**, 72

- Kriek, M., van Dokkum, P. G., Franx, M., et al. 2007, *ApJ*, **669**, 776
- Kriek, M., van Dokkum, P. G., Labbé, I., et al. 2009, *ApJ*, **700**, 221
- Kroupa, P. 2001, *MNRAS*, **322**, 231
- Lacy, M., Petric, A. O., Sajina, A., et al. 2007, *AJ*, **133**, 186
- Law, D. R., Steidel, C. C., Erb, D. K., et al. 2007, *ApJ*, **669**, 929
- Law, D. R., Steidel, C. C., Erb, D. K., et al. 2009, *ApJ*, **697**, 2057
- Law, D. R., Steidel, C. C., Shapley, A. E., et al. 2012, *ApJ*, **745**, 85
- Leitherer, C., Schaerer, D., Goldader, J. D., et al. 1999, *ApJS*, **123**, 3
- Lemoine-Busserolle, M., & Lamareille, F. 2010, *MNRAS*, **402**, 2291
- Levesque, E. M., Kewley, L. J., & Larson, K. L. 2010, *AJ*, **139**, 712
- Lilly, S. J., Carollo, C. M., Pipino, A., Renzini, A., & Peng, Y. 2013, *ApJ*, **772**, 119
- Lilly, S. J., Le Fèvre, O., Renzini, A., et al. 2007, *ApJS*, **172**, 70
- Liu, X., Shapley, A. E., Coil, A. L., Brinchmann, J., & Ma, C.-P. 2008, *ApJ*, **678**, 758
- Mancini, C., Foerster Schreiber, N., Renzini, A., et al. 2011, *ApJ*, **743**, 86
- Meynet, G., Maeder, A., Schaller, G., Schaerer, D., & Charbonnel, C. 1994, *A&AS*, **103**, 97
- Mignoli, M., Cimatti, A., Zamorani, G., et al. 2005, *A&A*, **437**, 883
- Miller, N. A., Fomalont, E. B., Kellermann, K. I., et al. 2008, *ApJS*, **179**, 114
- Newman, S. F., Genzel, R., Förster Schreiber, N. M., et al. 2013, *ApJ*, **767**, 104
- Newman, S. F., Shapiro Griffin, K., Genzel, R., et al. 2012, *ApJ*, **752**, 111
- Pauldrach, A. W. A., Hoffmann, T. L., & Lennon, M. 2001, *A&A*, **375**, 161
- Peng, C. Y., Ho, L. C., Impey, C. D., & Rix, H.-W. 2002, *AJ*, **124**, 266
- Pettini, M., & Pagel, B. E. J. 2004, *MNRAS*, **348**, L59
- Rangel, C., Nandra, K., Laird, E. S., & Orange, P. 2013, *MNRAS*, **428**, 3089
- Renzini, A., & da Costa, L. N. 1997, *Msngr*, **87**, 23
- Rich, J. A., Dopita, M. A., Kewley, L. J., & Rupke, D. S. N. 2010, *ApJ*, **721**, 505
- Rich, J. A., Kewley, L. J., & Dopita, M. A. 2011, *ApJ*, **734**, 87
- Rodighiero, G., Daddi, E., Baronchelli, I., et al. 2011, *ApJL*, **739**, L40
- Seifert, W., Ageorges, N., Lehmitz, M., et al. 2010, *Proc. SPIE*, **7735**, 77357W
- Shapiro, K. L., Genzel, R., Förster Schreiber, N. M., et al. 2008, *ApJ*, **682**, 231
- Shapley, A. E., Steidel, C. C., Erb, D. K., et al. 2005, *ApJ*, **626**, 698
- Steidel, C. C., Shapley, A. E., Pettini, M., et al. 2004, *ApJ*, **604**, 534
- Stern, D., Eisenhardt, P., Gorjian, V., et al. 2005, *ApJ*, **631**, 163
- Swinbank, A. M., Sobral, D., Smail, I., et al. 2012a, *MNRAS*, **426**, 935
- Swinbank, M., Smail, I., Sobral, D., et al. 2012b, *ApJ*, **760**, 130
- Tecza, M., Baker, A. J., Davies, R. I., et al. 2004, *ApJL*, **605**, L109
- Tremonti, C. A., Heckman, T. M., Kauffmann, G., et al. 2004, *ApJ*, **613**, 898
- Trump, J. R., Konidaris, N. P., Barro, G., et al. 2013, *ApJL*, **763**, L6
- Trump, J. R., Weiner, B. J., Scarlata, C., et al. 2011, *ApJ*, **743**, 144
- van den Bergh, S., Abraham, R. G., Ellis, R. S., et al. 1996, *AJ*, **112**, 359
- van Dokkum, P. G., Kriek, M., Rodgers, B., Franx, M., & Puxley, P. 2005, *ApJL*, **622**, L13
- van Starckenburg, L., van der Werf, P. P., Franx, M., et al. 2008, *A&A*, **488**, 99
- Vázquez, G. A., & Leitherer, C. 2005, *ApJ*, **621**, 695
- Veilleux, S., Cecil, G., & Bland-Hawthorn, J. 2005, *ARA&A*, **43**, 769
- Wisnioski, E., Glazebrook, K., Blake, C., et al. 2012, *MNRAS*, **422**, 3339
- Wright, S. A., Larkin, J. E., Barczys, M., et al. 2007, *ApJ*, **658**, 78
- Wright, S. A., Larkin, J. E., Graham, J. R., & Ma, C.-P. 2010, *ApJ*, **711**, 1291
- Wright, S. A., Larkin, J. E., Law, D. R., et al. 2009, *ApJ*, **699**, 421
- Wuyts, S., Förster Schreiber, N. M., Genzel, R., et al. 2012, *ApJ*, **753**, 114
- Wuyts, S., Förster Schreiber, N. M., van der Wel, A., et al. 2011, *ApJ*, **742**, 96
- Wuyts, S., Labbé, I., Schreiber, N. M. F., et al. 2008, *ApJ*, **682**, 985
- Xue, Y. Q., Luo, B., Brandt, W. N., et al. 2011, *ApJS*, **195**, 10
- Yabe, K., Ohta, K., Iwamuro, F., et al. 2012, *PASJ*, **64**, 60
- Yuan, T.-T., Kewley, L. J., & Rich, J. 2013a, *ApJ*, **767**, 106
- Yuan, T.-T., Kewley, L. J., & Richard, J. 2013b, *ApJ*, **763**, 9